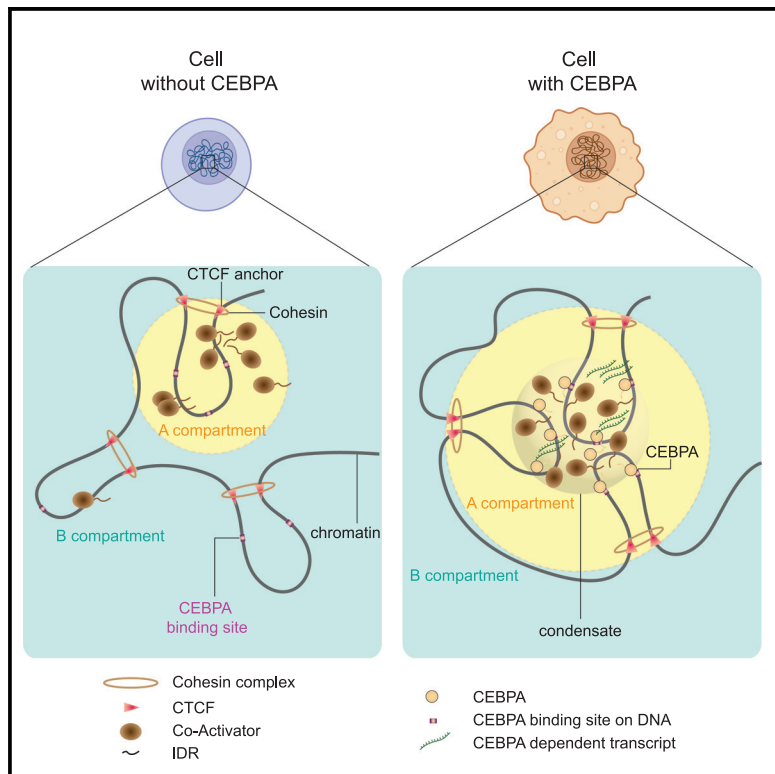


## CEBPA phase separation links transcriptional activity and 3D chromatin hubs

### Graphical abstract



### Authors

Marie Christou-Kent, Sergi Cuartero, Carla Garcia-Cabau, ..., Xavier Salvatella, Thomas Graf, Grégoire Stik

### Correspondence

thomas.graf@crg.eu (T.G.),  
gstik@carrerasresearch.org (G.S.)

### In brief

Christou-Kent et al. demonstrate that myeloid factor CEBPA undergoes phase separation (PS) through its intrinsically disordered region *in vitro*. The authors suggest that a PS mechanism may contribute to its capacity to rewire higher-order chromatin and modulate gene expression by bringing chromatin sites together at transcriptionally active hubs.

### Highlights

- CEBPA drives compartment switching and forms active 3D chromatin “hubs” in B cells
- Aromatic residues in the CEBPA-IDR confer phase separation capacity *in vitro*
- CEBPA forms hubs that colocalize with transcriptional co-activators in a native cell context
- Findings suggest a mechanistic role for phase separation in CEBPA function



## Report

# CEBPA phase separation links transcriptional activity and 3D chromatin hubs

Marie Christou-Kent,<sup>1,9</sup> Sergi Cuartero,<sup>2,3,9</sup> Carla Garcia-Cabau,<sup>4,9</sup> Julia Ruehle,<sup>1</sup> Julian Naderi,<sup>5</sup> Julia Erber,<sup>1</sup> Maria Victoria Neguembor,<sup>1</sup> Marcos Plana-Carmona,<sup>1</sup> Marc Alcoverro-Bertran,<sup>2</sup> Luisa De Andres-Aguayo,<sup>1</sup> Antonios Klonizakis,<sup>1</sup> Eric Julià-Vilella,<sup>2</sup> Cian Lynch,<sup>4,6</sup> Manuel Serrano,<sup>4,6</sup> Denes Hnisz,<sup>5</sup> Xavier Salvatella,<sup>4,7</sup> Thomas Graf,<sup>1,8,\*</sup> and Grégoire Stik<sup>2,10,\*</sup>

<sup>1</sup>Centre for Genomic Regulation (CRG), The Barcelona Institute of Science and Technology, Dr. Aiguader 88, 08003 Barcelona, Spain

<sup>2</sup>Josep Carreras Leukaemia Research Institute (IJC), Badalona, Spain

<sup>3</sup>Germans Trias i Pujol Research Institute (IGTP), Badalona, Spain

<sup>4</sup>Institute for Research in Biomedicine (IRB Barcelona), The Barcelona Institute of Science and Technology, Baldiri Reixac 10, 08028 Barcelona, Spain

<sup>5</sup>Department of Genome Regulation, Max Planck Institute for Molecular Genetics, Ihnestrasse 63-73, 14195 Berlin, Germany

<sup>6</sup>Altos Labs, Cambridge Institute of Science, Cambridge CB21 6GP, UK

<sup>7</sup>ICREA, Passeig Lluís Companys 23, 08010 Barcelona, Spain

<sup>8</sup>Universitat Pompeu Fabra (UPF), Barcelona, Spain

<sup>9</sup>These authors contributed equally

<sup>10</sup>Lead contact

\*Correspondence: [thomas.graf@crg.eu](mailto:thomas.graf@crg.eu) (T.G.), [gstik@carrerasresearch.org](mailto:gstik@carrerasresearch.org) (G.S.)

<https://doi.org/10.1016/j.celrep.2023.112897>

## SUMMARY

Cell identity is orchestrated through an interplay between transcription factor (TF) action and genome architecture. The mechanisms used by TFs to shape three-dimensional (3D) genome organization remain incompletely understood. Here we present evidence that the lineage-instructive TF CEBPA drives extensive chromatin compartment switching and promotes the formation of long-range chromatin hubs during induced B cell-to-macrophage transdifferentiation. Mechanistically, we find that the intrinsically disordered region (IDR) of CEBPA undergoes *in vitro* phase separation (PS) dependent on aromatic residues. Both overexpressing B cells and native CEBPA-expressing cell types such as primary granulocyte-macrophage progenitors, liver cells, and trophectoderm cells reveal nuclear CEBPA foci and long-range 3D chromatin hubs at CEBPA-bound regions. In short, we show that CEBPA can undergo PS through its IDR, which may underlie *in vivo* foci formation and suggest a potential role of PS in regulating CEBPA function.

## INTRODUCTION

The three-dimensional (3D) organization of the genome has emerged as a key element of transcriptional control.<sup>1–6</sup> Chromatin interactions are segregated into transcriptionally active (A) and inactive (B) compartments,<sup>7</sup> and dynamic processes such as differentiation<sup>8,9</sup> or reprogramming<sup>10,11</sup> entail extensive compartment switching, suggesting that compartmentalization may be a critical factor in cell fate transitions.<sup>12</sup> These transitions are mainly driven by the action of lineage-instructive transcription factors (TFs), which can activate entire transcriptional programs to shape cell identity.<sup>13,14</sup> As TF binding is associated with the modulation of distal interactions between enhancers and promoters, it has been proposed that TFs may be responsible for shaping higher-order genome architecture.<sup>3,15,16</sup> However, the mechanisms used by TFs to promote large-scale changes in genome architecture remain incompletely understood.<sup>3,16</sup>

Phase separation (PS) is the process underlying the formation of biomolecular condensates through numerous, weak interac-

tions between multivalent biomolecules.<sup>17,18</sup> Theoretical models have proposed that PS of transcriptional co-activators drives enhancer cooperativity and super-enhancer formation.<sup>19</sup> Supporting this hypothesis, multiple intrinsically disordered region (IDR)-containing TFs have been shown to form condensates and to co-condense with members of the general transcription machinery.<sup>20–22</sup> However, TFs can also perform their function at concentrations lower than those required for PS by nucleation on chromatin.<sup>22–25</sup> Further evidence indicates a role of PS in the formation of chromatin subcompartments.<sup>26</sup> This model may also imply an instrumental role of TFs in shaping higher-order chromatin structures such as compartments.

CCAAT enhancer binding protein alpha (CEBPA) is a TF required for myeloid specification,<sup>27,28</sup> hematopoietic stem cell (HSC) maintenance, and adipocyte and hepatocyte differentiation.<sup>29–31</sup> CEBPA contains three transactivation domains in the N-terminal region and a basic leucine zipper (bZIP) in the C-terminal region, which binds to DNA and dimerizes with other bZIP proteins.<sup>32</sup> Ectopic expression of CEBPA induces the transdifferentiation of B cells into macrophages.<sup>33</sup> We have previously



developed a B-ALL leukemia cell line (BLaER) with  $\beta$ -estradiol-inducible CEBPA expression that gives rise to functional macrophages within 168 h.<sup>34</sup> This system represents a suitable model to investigate how TF-induced genome topological changes relate to transcriptional control and cell fate transitions. Here, we found that CEBPA binding is associated to extensive compartment switching and promotes the establishment of long-range genomic interactions. Furthermore, we show that the IDR of CEBPA forms phase-separated condensates *in vitro* through interactions involving aromatic residues and accumulates in nuclear foci *in vivo* in different biological systems. These findings support a model in which CEBPA instructs cell fate decisions by rearranging 3D genome organization and inducing transcriptional changes.

## RESULTS

### CEBPA drives B to A compartment switching and long-range chromatin convergence during B cell to macrophage transdifferentiation

We investigated the interplay between CEBPA binding and genome architecture during the CEBPA-induced transdifferentiation of B cells into induced macrophages (iMacs) (Figure 1A). Using existing ChIP-sequencing data for CEBPA binding,<sup>35</sup> we determined genomic regions corresponding to CEBPA peaks 24 h post induction (Figure 1B). We selected this early time point since CEBPA is already bound to chromatin, while any potential indirect effects from additional upregulated myeloid factors are minimized. CEBPA binding is predominantly associated to regions 5–500 kb up- or downstream of transcription start sites (TSSs), indicating enhancer-related and/or structural roles (Figure 1C). Accordingly, 75% of CEBPA peaks were associated with multiple genes, and some binding was transient since many of the sites occupied by CEBPA at 24 h were devoid of CEBPA in iMacs (Figures S1A and S1B). Genes near CEBPA binding sites exhibited slightly higher expression and increased occupancy of H3K27ac and BRD4 (Figures 1D and S1C–S1G), supporting a link between CEBPA binding and transcriptional activation.

We previously performed Hi-C analyses at various time points after CEBPA induction and segregated chromatin into A and B compartments.<sup>35</sup> Combining these data with CEBPA ChIP-seq data showed that CEBPA binds mostly to A compartment chromatin upon induction. However, looking only at “dynamic” regions that switch compartments during transdifferentiation, we found that CEBPA binds more frequently than expected by chance to regions that switch from B to A compartments (Figure 1E), consistent with chromatin opening. An example of this is the JUN/FGGY locus that undergoes B to A compartment switching upon CEBPA binding (Figure 1F). We observed that CEBPA-bound sites formed local interactions within this region upon CEBPA induction and that these sites are associated with the active enhancer mark H3K27ac (Figure S1H). Of note, the vast majority of CEBPA peaks map to regulatory elements, particularly enhancers, and few overlap with peaks of the CCCTC-binding factor CTCF (Figure 1G). We generated aggregate heatmaps of normalized genome-wide Hi-C contacts centered on CEBPA binding sites 24 h post induction to explore

long-range interactions beyond TAD interactions (2–10 Mb). We observed a clear enrichment in long-range interactions between CEBPA-bound sites that was absent in non-induced cells (Figure 1H). Importantly, these interactions were detected even when CEBPA peaks did not overlap with CTCF peaks and persisted in the context of acute CTCF depletion (Figures S1I and S1J),<sup>35</sup> implying a loop extrusion-independent mechanism. These results suggest a mechanism whereby CEBPA binding drives chromatin opening and the convergence of specific sites, giving rise to transient, transcriptionally active hubs during the transdifferentiation of B cells. It has been proposed that transcriptional activators, including TFs, can converge through PS.<sup>19,20,36</sup> We therefore asked whether CEBPA is involved in the formation of transcriptional condensates (Figure S1K).

### CEBPA undergoes IDR-mediated phase separation *in vitro*

CEBPA contains a large IDR, encompassing over 70% of its sequence according to Metapredict and AlphaFold scores of disorder and structure (Figure 2A), which may enable PS. To test this hypothesis, we assessed the capacity of recombinant full-length (FL) CEBPA to undergo *in vitro* PS (in the presence of double-stranded DNA to avoid misfolding of the DNA binding domain). We observed that CEBPA-FL forms small clusters in the presence of crowding agent, reminiscent of droplets produced by PS (Figure 2B). To determine the role of the IDR, we produced recombinant CEBPA-IDR (residues 1–255) and CEBPA- $\Delta$ IDR (lacking residues 1–255) fused to mEGFP. CEBPA-IDR-mEGFP showed droplet formation, while CEBPA- $\Delta$ IDR-mEGFP did not, indicating that the IDR is responsible for CEBPA PS in these conditions (Figure 2B). Homotypic PS of CEBPA-IDR-mEGFP resulted in larger droplets with increasing protein concentration (Figures 2C and S2A) and was favored at high ionic strength and high temperature, indicating that the process is entropically favored and likely driven, at least in part, by hydrophobic intermolecular interactions<sup>37</sup> (Figure S2B). These droplets showed fusion events, and their formation was reversible upon crowding agent dilution (Figures S2C and S2D), indicating that the molecules are rapidly rearranging and sensitive to crowding.

To investigate whether CEBPA forms foci in the nuclear environment, we engineered the human B cell line RCH-ACV-rTA with doxycycline-inducible CEBPA-mEGFP expression (Figure 2D). In these overexpression conditions, live-cell imaging showed large CEBPA nuclear puncta in non-dense chromatin regions, the number of which correlated with the mean fluorescence intensity per cell (Figures S2E and S2F). These puncta exhibited rapid fluorescence recovery within seconds after photobleaching (Figures 2E and 2F), at rates comparable to those reported for other phase separating proteins.<sup>38,39</sup> Similar properties were observed in HepG2 (human liver cells chosen for a native CEBPA expression context) overexpressing CEBPA-mEGFP, which forms puncta that recover rapidly after photobleaching in comparison to control mEGFP (Figures S2G and S2H).

Numerous TFs have been shown to be able to form heterotypic condensates with transcriptional co-activators such as BRD4 and MED1, suggestive of a role in transcription activation.<sup>20,21,40</sup> To test whether this holds true for CEBPA, we produced MED1-IDR

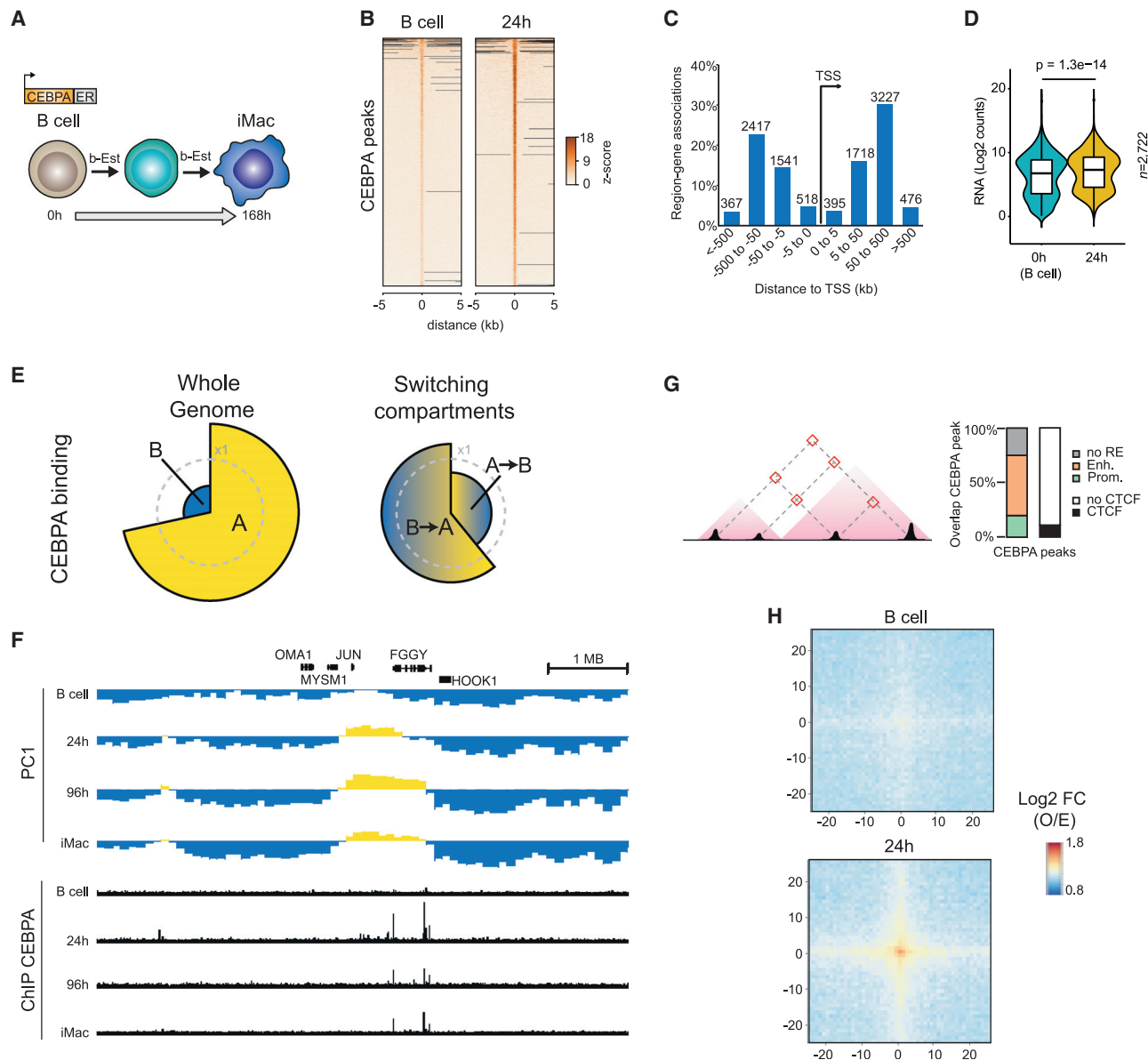


**Figure 1. CEBPA drives B to A compartment switching and long-range chromatin convergence during B cell to macrophage transdifferentiation**

(A) CEBPA fused with estrogen receptor (CEBPA-ER) translocates to the nucleus after  $\beta$ -estradiol (b-Est) treatment, converting B-ALL cells into induced macrophages ("iMacs").

(B) Heatmap of CEBPA binding centered on CEBPA peaks detected 24 h after CEBPA induction. Black lines represent segments of the genome with no read coverage.

(C) Frequency of the genomic distance (in kb) to transcription start sites (TSSs) of CEBPA-binding sites.

(D) RNA levels of genes in proximity (<50 kb) to CEBPA peaks (defined at 24 h CEBPA expression) at 0 and 24 h CEBPA (n represents the number of genes, and p values are calculated using a two-sided Wilcoxon rank-sum test).

(E) Combined pie chart and radar plot depicting the proportion of CEBPA binding to A or B compartments genome-wide (left) and in "switching chromatin compartment" (right). The height of each pie segment indicates fold enrichment (denoted by the gray circles) showing a specific CEBPA binding in B to A switching compartments during B cell to macrophage differentiation. The gray dashed circle represents enrichment of 1.

(F) CEBPA binding (black tracks) and compartment switching (PC1 values, Hi-C, blue and yellow representing B and A compartment, respectively) at the JUN/FGGY locus during the transdifferentiation of B cells to iMacs.

(G) Left: schematic representation of the Hi-C meta-analysis performed at CEBPA peaks. Right: overlap of CEBPA peaks with regulatory elements (REs) and CTCF peaks (Enh., enhancer; Prom., promoter).

(H) Aggregate heatmaps of normalized interactions (2–10 Mbp) between CEBPA peaks at 0 and 24 h of CEBPA induction (O/E, observed over expected), showing 250 kb upstream and downstream of the bound regions at 10-kb resolution. See also [Figure S1](#).

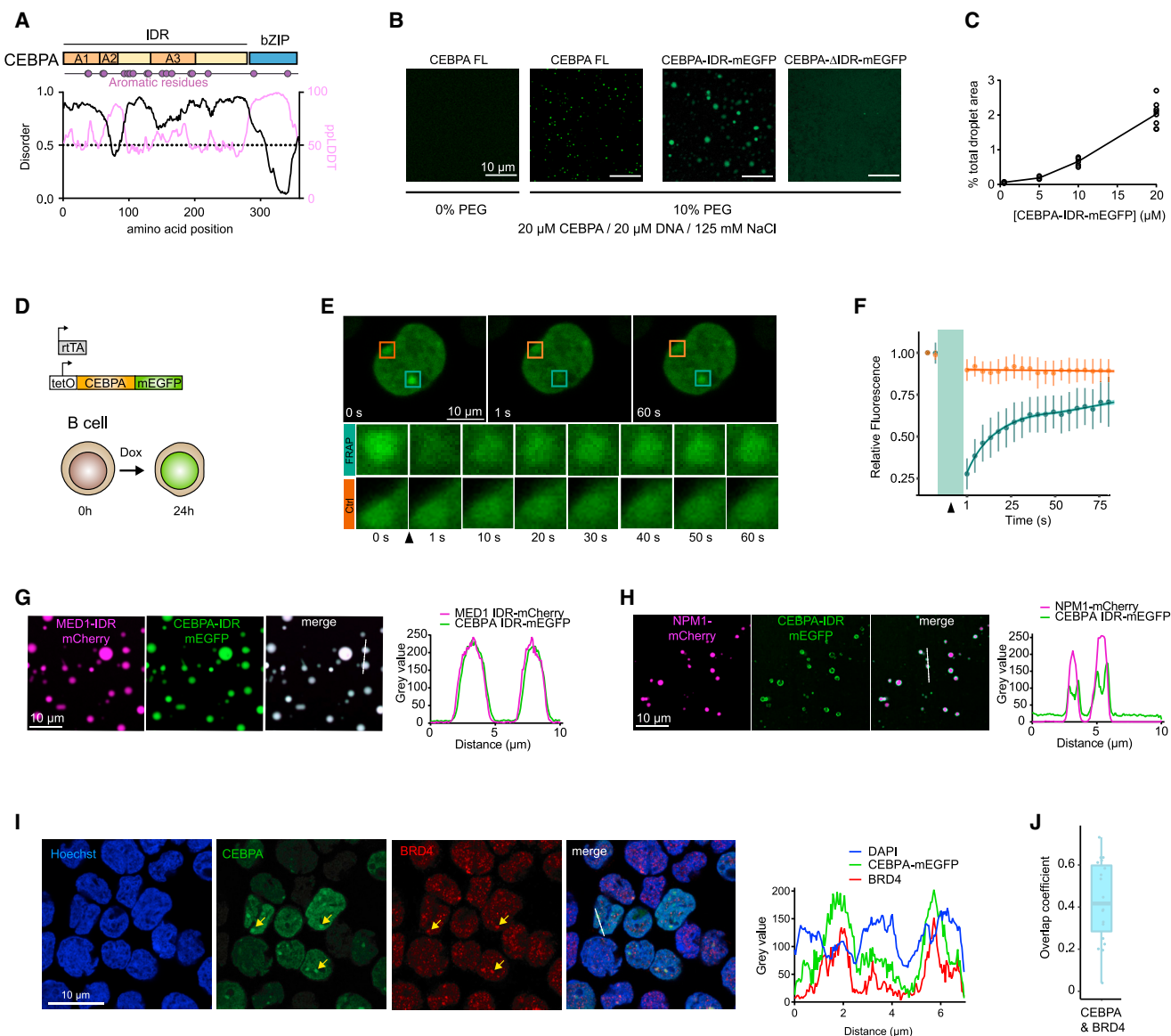


**Figure 2. CEBPA undergoes IDR-mediated phase separation *in vitro***

(A) Upper: map of CEBPA depicting the location of aromatic residues, intrinsically disordered region (IDR), three activation domains (A1–3), and basic leucine zipper (bZIP) DNA binding domain. Lower: Metapredict disorder scores and AlphaFold structure scores (ppIDDT).

(B) Phase separation of FL-CEBPA (labeled with DyLight 488), CEBPA-IDR-mEGFP, and CEBPA-ΔIDR-mEGFP recombinant protein (CEBPA 20 μM, DNA 20 μM, 125 mM NaCl).

(C) Phase separation of recombinant CEBPA-IDR-mEGFP measured by quantification of total droplet area relative to protein concentration (10% PEG 4000, 125 mM NaCl).

(D) Schematic representation of a B cell expressing doxycycline-inducible CEBPA-mEGFP.

(E) Fluorescence recovery after photobleaching of 24-h CEBPA-mEGFP-induced B cells. Green box: photobleached punctum. Orange box: control punctum.

(F) Relative fluorescence for photobleached and unbleached puncta normalized against non-photobleached puncta and background intensity (n = 12).

(G and H) Co-condensates of CEBPA-IDR-mEGFP and MED1-IDR-mCherry recombinant proteins and (H) unblended droplets formed when mixing CEBPA-IDR-mEGFP and NPM1-mCherry. Line scan analyses of the merged pictures are depicted on the right. Proteins at 5 μM.

(I) CEBPA-mEGFP-transduced B cells immunostained for BRD4. Yellow arrows indicate co-localized CEBPA and BRD4 puncta. A line scan analysis of the merged image is depicted on the right.

(J) Quantification showing the overlap of CEBPA-mEGFP puncta with BRD4 puncta. See also Figure S2.

tagged with either mCherry or EBFP2. CEBPA-IDR-mEGFP readily formed heterotypic condensates with MED1-IDR-mCherry, which were larger than those observed with CEBPA-IDR-mEGFP alone (Figures 2G and S2A). CEBPA-IDR-mEGFP was also able to form heterotypic condensates with PU1-mCherry, an important co-regulator of CEBPA in

myelopoiesis,<sup>33,41,42</sup> and PPARG2-mCherry, an adipocyte TF that is upregulated by CEBPA during fat cell differentiation,<sup>43</sup> forming round condensates with both in the presence of MED1-IDR-EBFP2 (Figure S2I). In contrast, CEBPA did not co-condense with NPM1-mCherry, a nucleolar protein that undergoes PS via electrostatic rather than hydrophobic forces (Figure 2H).

We next investigated by immunostaining whether CEBPA foci colocalize with functionally related TFs and co-activators in CEBPA-overexpressing B cells (Figures 2I and S2J). Co-localization coefficients showed a high degree of overlap of CEBPA-mEGFP with BRD4 and IKAROS but not with EBF1 puncta (Figures 2J and S2K). This could be explained by the fact that IKAROS, like CEBPA, has a role in myeloid differentiation, whereas the function of EBF1 is restricted to B cell specification.<sup>44,45</sup> To obtain a more accurate view of the CEBPA subnuclear distribution we performed stochastic optical reconstruction microscopy using induced B cells. This revealed hundreds of discrete clusters not resolved by conventional confocal microscopy (Figures S2L and S2M). These clusters were larger at higher protein concentration as visible when comparing the size of clusters inside the nucleus and in the residual cytosolic fraction (Figures S2N and S2O). Therefore, the larger CEBPA-mEGFP foci observed in CEBPA-overexpressing B cells by confocal microscopy are likely to be, in fact, conglomerates of many smaller puncta that are visible only by super-resolution microscopy.

#### ***trans* and *cis* mutations of CEBPA impaired its phase separation capacity, transcriptional activity, and ability to rewire chromatin**

Aromaticity is emerging as a biophysical determinant of the ability of activation domains to activate transcription<sup>46</sup> and, in specific cases, phase separate *in vitro* and in cells.<sup>47–49</sup> To investigate whether the aromaticity of CEBPA determines its PS propensity, we generated an IDR mutant CEBPA construct in which all 16 aromatic residues (7 tyrosines and 9 phenylalanines) within the IDR were substituted by alanine residues (named AroLITE) (Figure 3A). We observed that recombinant CEBPA AroLITE-IDR-mEGFP lacked the capacity to undergo PS at all salt and protein concentrations, temperatures, and crowding agents tested (Figures 3B, 3C, and S3A), confirming that CEBPA homotypic PS is driven by interactions involving aromatic residues in its IDR. The AroLITE-IDR-mEGFP was nonetheless able to partition into pre-assembled MED1-IDR-mCherry droplets (Figure 3D) but less efficiently than for wild-type (WT)-IDR-mEGFP (Figures 3E and 3F). The AroLITE-CEBPA was also strongly impaired in its capacity to form heterotypic condensates with PU1 and in its transactivation capacity in the GAL4-DBD-luciferase system compared to the WT (Figures S3B–S3E). These data indicate that the ability of CEBPA to co-condense with transcriptional partners is partially mediated through aromatic residues in the IDR.

We next transduced human B cells (RCH-ACV-rtTA) with Dox-inducible FL CEBPA AroLITE. While the stability of the protein was intact (Figure S3F), the AroLITE substitutions impaired the upregulation of macrophage genes including CSF1R, ITGAM, FCGRI, CD14, and PU1 and the downregulation of B cell genes EBF1 and VPREF3 24 h post induction (Figures 3G and S3G). We

hypothesized that these effects could be attributed to perturbation in CEBPA-driven mediation of genomic interactions via its IDR. However, we cannot exclude the possibility that the AroLITE-IDR substitutions may have multiple effects beyond PS since CEBPA is known to interact with transcriptional complexes such as SWI/SNF and TBP/TFIIB<sup>50</sup> through its IDR. To specifically assess the role of CEBPA in mediating long-range interactions without perturbing its amino acid sequence, we used CRISPR-Cas9 to knock out an ~500-bp region containing a CEBPA binding site located in the JUN/FGGY region that undergoes compartment switching after CEBPA induction in B cells (Figures 3H, S3H, and S3I; see also Figure 1F). The impact of the deletion on the conformation of the region was measured by *in situ* Hi-C, which revealed that the compartmental repositioning was altered in the knockout (KO) cells specifically around the targeted CEBPA site (Figure 3I). Of note, this alteration of large-scale chromatin conformation dynamics was accompanied by a slight perturbation of local interactions within the region harboring the KO CEBPA peak, evidenced by decreased interactions with surrounding bins containing CEBPA peaks (Figure S3J).

#### **Native CEBPA drives the formation of nuclear foci**

To rule out possible artifactual observations due to overexpression conditions, we asked whether CEBPA localizes at visible nuclear foci when expressed at endogenous levels. Among hematopoietic cell types, CEBPA is moderately expressed in HSCs and common myeloid progenitors, highly expressed in granulocyte/monocyte progenitors (GMPs), and depleted in megakaryocyte-erythroid progenitors (MEPs) (Figures 4A and 4B).<sup>51</sup> We immunostained primary GMPs from the bone marrow of transgenic mice constitutively expressing MED1 tagged with GFP. Super-resolution imaging showed CEBPA nuclear foci of varying size that partially colocalize with MED1 foci (Figure 4C), demonstrating that endogenous CEBPA forms nuclear foci in a native cellular context, potentially compatible with transcriptional condensates. Notably, the level of co-localization of CEBPA with MED1 was comparable to the one observed between MED1 and BRD4 but substantially higher than with the heterochromatic protein HP1a (Figures 4C, S4A, and S4B). The incomplete degree of overlap between MED1 and CEBPA or BRD4 is consistent with what has been observed with Mediator and OCT4 in embryonic stem cells,<sup>20</sup> potentially reflecting transient interactions or epitope availability.

Using Hi-C data from several hematopoietic cell types<sup>52</sup> and a GMP CEBPA ChIP-seq dataset,<sup>30</sup> we analyzed the A/B segmentation of the regions to which CEBPA binds in GMPs and computed the corresponding first component of a principal components analysis (PC1) values of these regions in HSCs, MEPs, and GMPs. We then devised categories according to the compartment status of each site across the three cell types (Figure 4D). The second largest category (after AAA, referring to sites in the A compartment in all cell types) was “ABA” (HSC-MEP-GMP), signifying sites that were in the A compartment in CEBPA-expressing HSCs and GMPs and in the B compartment in CEBPA-depleted MEPs. The average PC1 values of GMP CEBPA sites correlated with global CEBPA expression in the three cell types (Figure 4E). This effect is nicely exemplified

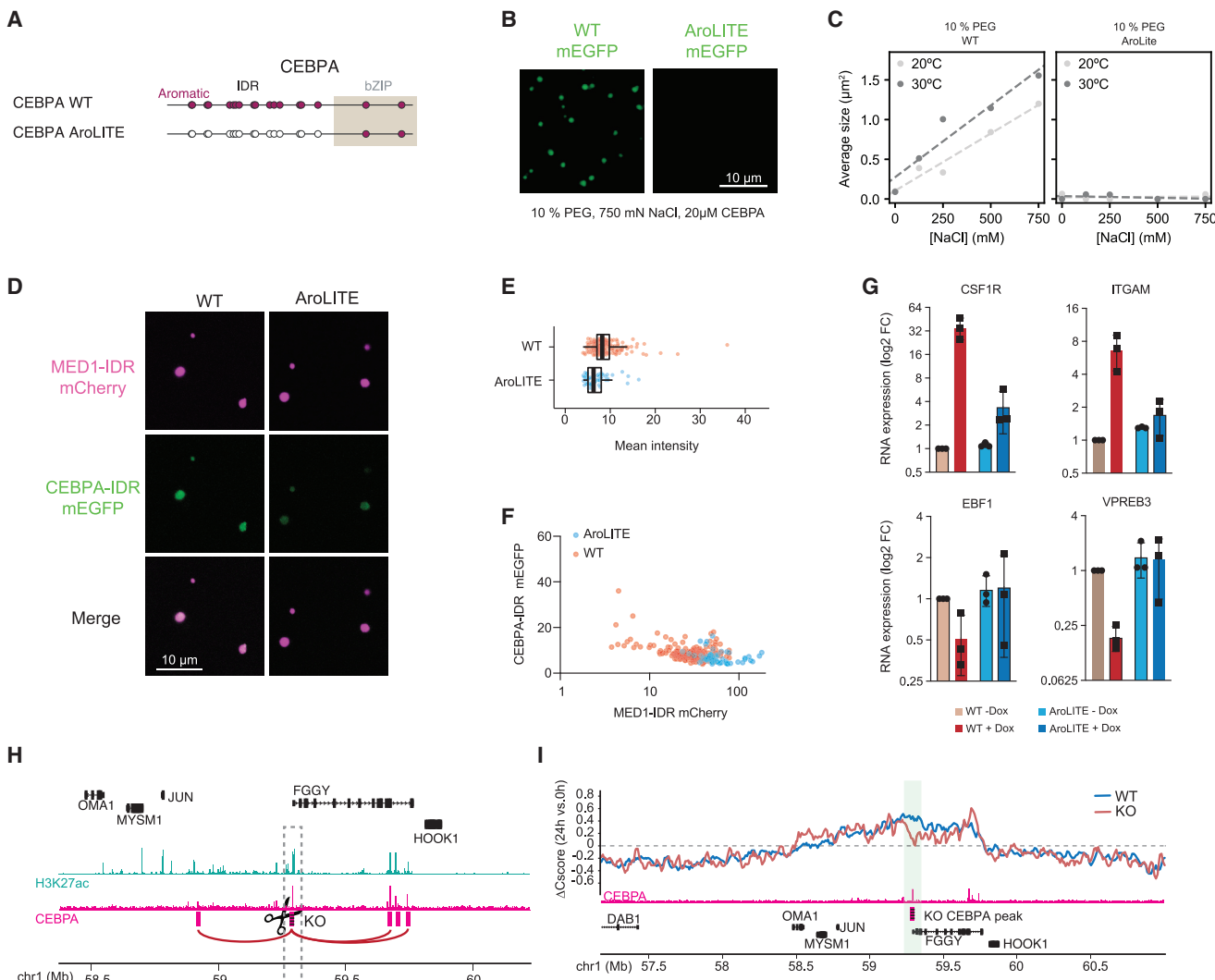


**Figure 3. *trans* and *cis* mutations of CEBPA impaired its *in vitro* phase separation capacity, transcriptional activity, and ability to rewire chromatin**

- (A) Location of aromatic residues in human CEBPA (red dots). White dots: aromatic residues mutated to alanine residues to create the AroLITE variant.
- (B) Droplets formed by recombinant CEBPA-IDR-WT and AroLITE mutant.
- (C) Average CEBPA-IDR-WT and -AroLITE droplet size according to salt concentration at 20°C and 30°C.
- (D) Partitioning of recombinant CEBPA-IDR-WT or -AroLITE mEGFP at 1 μM into pre-formed MED1 droplets at 10 μM.
- (E) Mean mEGFP fluorescence intensity within MED1-IDR-mCherry droplets for CEBPA-IDR-WT and AroLITE.
- (F) Scatterplot of MED1-IDR-mCherry mean intensity against WT and AroLITE-CEBPA-IDR-mEGFP mean intensity.
- (G) Expression levels measured by qRT-PCR of macrophage and B cell markers normalized to GUSB in B cells transduced with doxycycline-inducible CEBPA-WT or -AroLITE, with and without doxycycline treatment. Error bars represent mean ± standard deviation.
- (H) ChIP-seq tracks of H3K27ac (green) and CEBPA (pink) at the JUN/FGGY locus. Pink rectangles: CEBPA peaks. Gray dashed box: peak targeted for CRISPR KO. Red lines: significant Hi-C interactions between 10-kb bins harboring CEBPA peaks.
- (I) C-score changes at 24 h after CEBPA induction in WT (blue) and KO (red) B cells (10-kb resolution). Positive and negative values represent compartmental repositioning toward active A compartment and inactive B compartment, respectively. Pink: CEBPA ChIP-seq track and the excised CEBPA binding. Light blue box: region showing impaired compartmental repositioning in the KO. See also Figure S3.

around the *Tfec* and *Trps1* loci (Figures 4F and S4C), in which GMP CEBPA site-containing regions of several hundred kilobases in size are shown to undergo differential compartmental switching in GMPs and MEPs relative to HSCs. *Tfec* and *Trps1* expression levels in the three cell types corroborate these observations since both genes are silenced in MEPs and maintained or

upregulated in GMPs relative to HSCs (Figures 4G and S4D). Aggregate plots of Hi-C data centered on GMP CEBPA sites show strongly enriched long-range interactions between CEBPA-bound sites in GMPs, slightly enriched long-range interactions in HSCs, and absence of specific enrichment in MEPs (Figure 4H). In addition, the expression levels of genes in

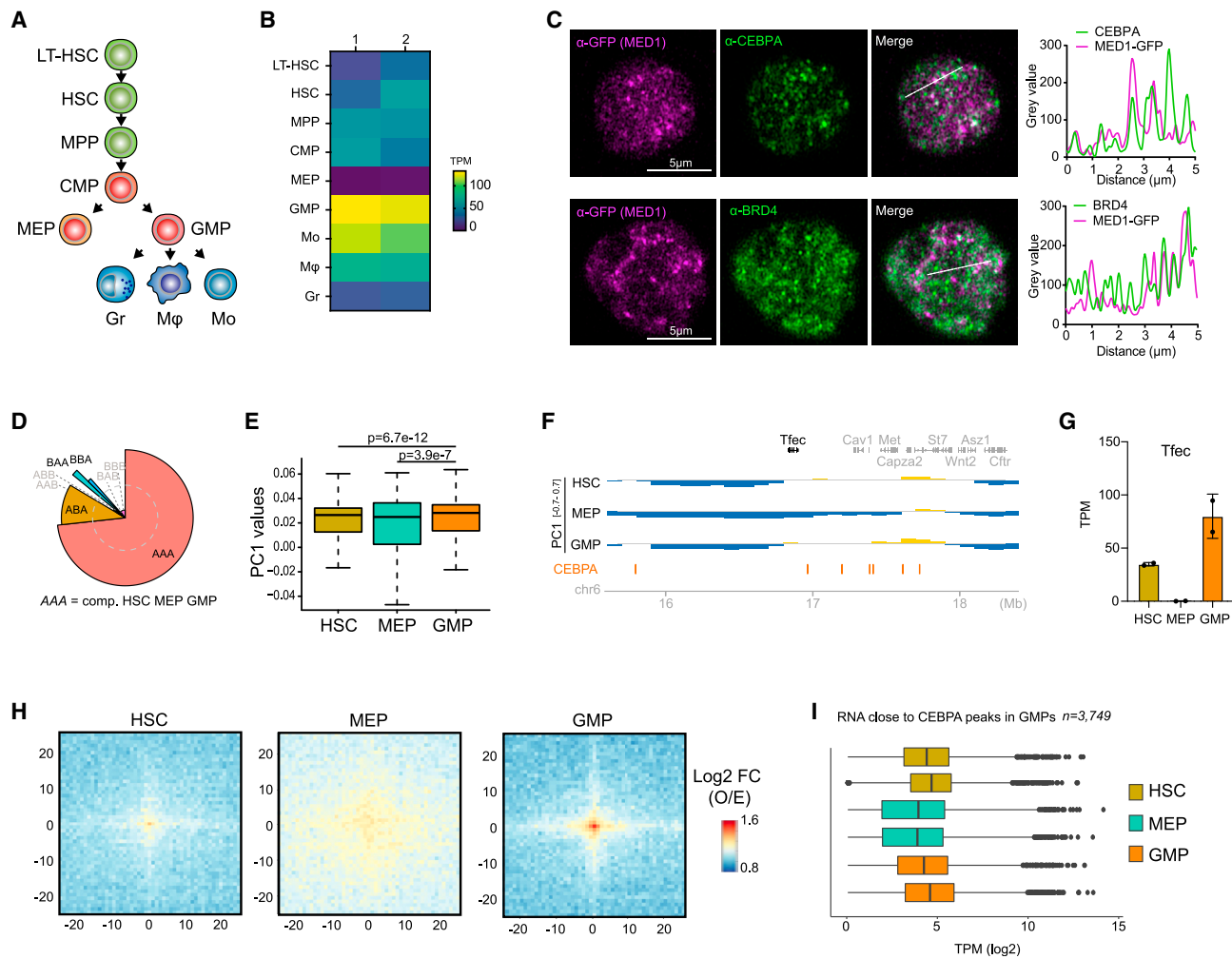


**Figure 4. CEBPA is enriched in active chromatin regions in hematopoietic cells**

(A) Myeloid differentiation. (LT)-HSC, (long-term) hematopoietic stem cell; MPP, multipotential progenitor; CMP, common myeloid progenitor; MEP, megakaryocyte/erythroid progenitor; GMP, granulocyte/monocyte progenitor; Mo, monocyte; Mφ, macrophage; Gr, granulocyte.

(B) CEBPA RNA expression data for hematopoietic cell types shown in Figure 4A. TPM, transcripts per million.

(C) Primary GMPs from MED1-GFP mice immunostained for GFP, CEBPA, or BRD4 and imaged at super resolution. Right: line scan analysis of the merged image.

(D) Sites bound by CEBPA in GMPs categorized according to A/B compartmentalization in HSCs, MEPs and GMPs, shown in that order. Pie chart shows the proportion of sites falling into each category (gray dashed circle shows the reference level for enrichment).

(E) Average PC1 values of GMP CEBPA site bins across the three indicated cell types (n = 3,573 bins, p values are calculated using a two-sided Wilcoxon rank-sum test).

(F) PC1 values in the region containing the gene *Tfec* across HSCs, MEPs, and GMPs. GMP CEBPA sites shown in orange.

(G) RNA expression of *Tfec* across the three hematopoietic cell types. Error bars represent mean ± standard deviation.

(H) Aggregate heatmaps of normalized interactions (2–10 Mbp) between CEBPA peaks in HSCs, MEPs, and GMPs centered on GMP CEBPA peaks (O/E = observed over expected), showing 250 kb up- and downstream of the bound regions at 10-kb resolution.

(I) RNA levels of genes in proximity (<50 kb) to CEBPA ChIP-seq peaks in GMPs. See also Figure S4.

proximity to CEBPA peaks are higher in GMPs and HSCs (Figure 4I), reflecting the trend observed for the 3D interconnectivity between CEBPA-bound chromatin regions, and the transcription level of genes associated with CEBPA also correlated with the peak score in GMPs (Figure S4E).

CEBPA is expressed in several cell lines derived from myeloid, liver, and placental cancers (Figure S4F). Moreover, we recently described the expression of CEBPA in the trophectoderm of blastocysts<sup>53</sup> and therefore immunostained mouse

blastocysts for CEBPA (Figure S4G). Trophectoderm cells showed small nuclear CEBPA puncta as well as larger conglomerates with a distribution distinct from chromatin-dense regions and splicing speckles (Figures S4H). Since CEBPA is functionally expressed in human hepatocytes,<sup>29</sup> we imaged the hepatocellular carcinoma-origin HepG2 cells.<sup>54</sup> Endogenous CEBPA exhibited a punctate nuclear staining pattern with higher colocalization with the co-activator P300 than with HP1a. (Figures S4I and S4J). Hi-C analyses of these cells

revealed enriched long-range interactions between CEBPA-bound sites and high BRD4 occupancy at CEBPA peaks (Figures S4K and S4L). Altogether, these data support the notion that, as observed in B cell to macrophage transdifferentiation, CEBPA drives the formation of chromatin hubs during hematopoiesis and development.

## DISCUSSION

In this study we employed an experimental setting that exploits the capacity of CEBPA to transdifferentiate B cells into macrophages.<sup>34,35,55</sup> We found that *de novo* CEBPA binding was associated with a rewiring of chromatin compartmentalization, driven through the establishment of new long-range interactions and coupled to the rapid activation of a myeloid program. The targeted deletion of a CEBPA binding site proved that CEBPA binding is required for the formation of such long-range 3D chromatin interactions, directly implicating CEBPA in 3D genome reorganization during cell fate transitions.

Mechanistically, we have identified the N-terminal disordered region of CEBPA as a driver of *in vitro* PS, adding to growing evidence that mammalian TFs exhibit PS capacity.<sup>20,21</sup> The substitution of aromatic residues within the IDR abolished the capacity of the CEBPA-IDR to undergo homotypic PS and impaired its ability to form shared condensates with both MED1 and PU.1 *in vitro*. CEBPA-IDR can therefore be classified with other TFs whose PS depends on aromatic interactions.<sup>56–59</sup> One possible interpretation of our data is that the capacity for *in vitro* PS of the CEBPA-IDR may play a significant role in its proper function during transcriptional activation. Nevertheless, a causal relationship between CEBPA-IDR PS and transcriptional activation requires further evidence. A possible alternative explanation for the transcriptional defects observed in AroLITE-expressing cells is that conformational changes in CEBPA hinder the formation of a complex with typical CEBPA partners, resulting in a dysfunctional complex. Further investigations using Hi-C and proteomics in AroLITE mutants will be crucial to address these questions.

Altogether, we propose a model in which the binding of CEBPA at distal gene enhancers drives long-range chromatin re-modeling and the convergence of bound sites in transcriptionally active hubs. Our data suggest that this occurs in B cell to macrophage transdifferentiation, in native hematopoiesis, in liver cells, and during early development. We show that CEBPA binding induces compartment switches, and this is paralleled by changes in gene expression. Our results evoke the intriguing possibility that the PS capacity of the CEBPA-IDR could play a part in these roles. However, the role of PS in compartmentalization is still mainly correlative. Further studies will be necessary to prove the causality of this process and to explore whether this mechanism is a general property of lineage-instructive TFs, which may ultimately be exploited for the development of therapies for developmental conditions and cancer.

### Limitations of the study

Proving the strict requirement of PS in the capacity of CEBPA to drive chromatin reorganization is complicated by the lack of precise tools to specifically inhibit PS without interfering with other

aspects of CEBPA function.<sup>60–63</sup> Currently, the only available tool, 1,6-hexanediol, has been criticized for its toxicity and potential artifacts.<sup>64–66</sup> Another limitation is that, while our experimental system allows the precise dissection of transcriptional and chromatin changes during transdifferentiation, it requires the overexpression of CEBPA to artificially high levels. We are also aware that alternative models, independent of a PS mechanism, could explain the transcriptional defects observed for the AroLITE mutant. For these reasons, although our data suggest a potential link between TF PS and the formation of transcriptional hubs, we are cautious not to overstate the causality of these phenomena.

## STAR METHODS

Detailed methods are provided in the online version of this paper and include the following:

- **KEY RESOURCES TABLE**
- **RESOURCE AVAILABILITY**
  - Lead contact
  - Materials availability
  - Data and code availability
- **EXPERIMENTAL MODEL AND STUDY PARTICIPANT DETAILS**
  - Cell culture
  - Mice models
- **METHOD DETAILS**
  - Mouse embryo culture
  - Obtaining primary GMPs
  - Generation of doxycycline-inducible CEBPA overexpression lines in RCH cells
  - Generation of DNA constructs for transactivation assays
  - Transactivation assay
  - CRISPR-Cas9 genome editing
  - RNA extraction and quantitative RT-PCR
  - Live cell imaging
  - Fluorescence Recovery After Photo bleaching (FRAP)
  - Immunostaining of RCH-ACV, HepG2, mouse embryos, primary GMP cells
  - Airyscan imaging
  - Co-localization analysis
  - Cell preparation and Immunolabeling for Stochastic Optical Reconstruction Microscopy (STORM) imaging
  - STORM imaging
  - STORM imaging analysis
  - Identification of intrinsically disordered protein regions
  - Generation of DNA constructs for protein purification
  - Protein purification
  - *In vitro* droplet assays
  - Partitioning of CEBPA into MED1 IDR droplets
  - Protein sequences
  - *In situ* Hi-C library preparation and initial data processing
  - Identification of subnuclear compartments
  - Long-range interactions between CEBPA binding regions

- Identification of differential interactions between non-induced and 24h CEBPA induced B cells
- CEBPA interaction at the JUN locus
- Gene expression analysis using RNA-seq data
- ChIP-seq data analysis

● **QUANTIFICATION AND STATISTICAL ANALYSIS**

**SUPPLEMENTAL INFORMATION**

Supplemental information can be found online at <https://doi.org/10.1016/j.celrep.2023.112897>.

**ACKNOWLEDGMENTS**

We thank the Graf lab members for helpful discussions, and the CRG Genomics, Flow Cytometry and Advanced Light Microscopy core facilities; M.C.-K. was supported by an EMBO postdoctoral fellowship (ALTF 1057-2019) and PCIN-MSCA-fellowship (Ministerio de Ciencia e Innovación PCI2021-122032-2B). S.C. is supported by a “La Caixa” Junior Leader fellowship, by the Jérôme Lejeune Foundation (JLF#1902) and the Spanish Ministry of Science and Innovation (PID2020-117950RA-I00). G.S. was supported by the “Fundación Científica de la Asociación Española Contra el Cáncer.” M.V.N. was supported by People Program (Marie Curie Actions) FP7/2007-2013 under REA grant 6089 and Juan de la Cierva-Incorporación 2017. C.G.-C. acknowledges a graduate fellowship from MINECO (PRE2018-084684). X.S. acknowledges funding from AGAUR (2017 SGR 324), MINECO (BIO2015-70092-R and PID2019-110198RB-I00), and the European Research Council (CONCERT, contract number 648201). This work was funded by the Max Planck Society and partially supported by grants from the Deutsche Forschungsgemeinschaft (DFG) SPP2202 Priority Program Grant HN 4/1-1 (to D.H.) and by the Spanish Ministry of Economy, Industry and Competitiveness (MEIC) Plan Estatal 2015, SAF.2015-68740-P (to T.G.). We acknowledge support by the Spanish Ministry of Science and Innovation, to the EMBL partnership, the Centro de Excelencia Severo Ochoa, the Josep Carreras Foundation, and the CERCA Programme / Generalitat de Catalunya.

**AUTHOR CONTRIBUTIONS**

Conceptualization, M.C.-K., S.C., C.G.-C., J.R., J.N., X.S., D.H., T.G., and G.S. Investigation, M.C.-K., S.C., C.G.-C., J.R., J.E., J.N., C.L., M.P.-C., M.A.-B., L.D.A.-A., E.J.-V., A.K., and G.S. Methodology, M.C.-K., S.C., T.G., and G.S. Resources, M.S., X.S., D.H., T.G., and G.S. Visualization, M.C.-K., S.C., J.R., C.G.-C., J.N., M.V.N., M.P.-C., M.A.-B., L.D.A.-A., E.J.-V., and G.S. Writing – original draft, M.C.-K., S.C., T.G., and G.S. Supervision, T.G. and G.S. Funding acquisition, X.S., D.H., T.G., and G.S.

**DECLARATION OF INTERESTS**

D.H. and X.S. are scientific founders and advisors of Nuage Therapeutics.

**INCLUSION AND DIVERSITY**

We support inclusive, diverse, and equitable conduct of research.

Received: June 28, 2022

Revised: June 2, 2023

Accepted: July 14, 2023

Published: July 29, 2023

**REFERENCES**

1. Bonev, B., and Cavalli, G. (2016). Organization and function of the 3D genome. *Nat. Rev. Genet.* 17, 661–678. <https://doi.org/10.1038/nrg.2016.112>.
2. Oudelaar, A.M., and Higgs, D.R. (2021). The relationship between genome structure and function. *Nat. Rev. Genet.* 22, 154–168. <https://doi.org/10.1038/S41576-020-00303-X>.
3. Stadhouders, R., Filion, G.J., and Graf, T. (2019). Transcription factors and 3D genome conformation in cell-fate decisions. *Nature* 569, 345–354. <https://doi.org/10.1038/s41586-019-1182-7>.
4. McCord, R.P., Kaplan, N., and Giorgetti, L. (2020). Chromosome Conformation Capture and Beyond: Toward an Integrative View of Chromosome Structure and Function. *Mol. Cell.* 77, 688–708. <https://doi.org/10.1016/J.MOLCEL.2019.12.021>.
5. Schoenfelder, S., and Fraser, P. (2019). Long-range enhancer–promoter contacts in gene expression control. *Nat. Rev. Genet.* 20, 437–455. <https://doi.org/10.1038/s41576-019-0128-0>.
6. Ibrahim, D.M., and Mundlos, S. (2020). The role of 3D chromatin domains in gene regulation: a multi-faceted view on genome organization. *Curr. Opin. Genet. Dev.* 61, 1–8. <https://doi.org/10.1016/J.GDE.2020.02.015>.
7. Lieberman-Aiden, E., van Berkum, N.L., Williams, L., Imakaev, M., Ragoczy, T., Telling, A., Amit, I., Lajoie, B.R., Sabo, P.J., Dorschner, M.O., et al. (2009). Comprehensive mapping of long-range interactions reveals folding principles of the human genome. *Science* 326, 289–293. <https://doi.org/10.1126/science.1181369>.
8. Dixon, J.R., Jung, I., Selvaraj, S., Shen, Y., Antosiewicz-Bourget, J.E., Lee, A.Y., Ye, Z., Kim, A., Rajagopal, N., Xie, W., et al. (2015). Chromatin architecture reorganization during stem cell differentiation. *Nature* 2015 518, 331–336. <https://doi.org/10.1038/nature14222>.
9. Bonev, B., Mendelson Cohen, N., Szabo, Q., Fritsch, L., Papadopoulos, G.L., Lubling, Y., Xu, X., Lv, X., Hugnot, J.P., Tanay, A., and Cavalli, G. (2017). Multiscale 3D Genome Rewiring during Mouse Neural Development. *Cell* 171, 557–572.e24. <https://doi.org/10.1016/J.CELL.2017.09.043>.
10. Krijger, P.H.L., Di Stefano, B., De Wit, E., Limone, F., van Oevelen, C., De Laat, W., and Graf, T. (2016). Cell-of-Origin-Specific 3D Genome Structure Acquired during Somatic Cell Reprogramming. *Cell Stem Cell* 18, 597–610. <https://doi.org/10.1016/j.stem.2016.01.007>.
11. Stadhouders, R., Vidal, E., Serra, F., di Stefano, B., le Dily, F., Quilez, J., Gomez, A., Collombet, S., Berenguer, C., Cuartero, Y., et al. (2018). Transcription factors orchestrate dynamic interplay between genome topology and gene regulation during cell reprogramming. *Nat. Genet.* 50, 238–249. <https://doi.org/10.1038/s41588-017-0030-7>.
12. Cuartero, S., Stik, G., and Stadhouders, R. (2023). Three-dimensional genome organization in immune cell fate and function. *Nat. Rev. Immunol.* 23, 206–221. <https://doi.org/10.1038/S41577-022-00774-5>.
13. Graf, T., and Enver, T. (2009). Forcing cells to change lineages. *Nature* 462, 587–594. <https://doi.org/10.1038/nature08533>.
14. Yamanaka, S., and Blau, H.M. (2010). Nuclear reprogramming to a pluripotent state by three approaches. *Nature* 465, 704–712. <https://doi.org/10.1038/NATURE09229>.
15. Johanson, T.M., Lun, A.T.L., Coughlan, H.D., Tan, T., Smyth, G.K., Nutt, S.L., and Allan, R.S. (2018). Transcription-factor-mediated supervision of global genome architecture maintains B cell identity. *Nat. Immunol.* 19 (19), 1257–1264. <https://doi.org/10.1038/s41590-018-0234-8>.
16. Kim, S., and Shendure, J. (2019). Mechanisms of Interplay between Transcription Factors and the 3D Genome. *Mol. Cell.* 76, 306–319. <https://doi.org/10.1016/J.MOLCEL.2019.08.010>.
17. Banani, S.F., Lee, H.O., Hyman, A.A., and Rosen, M.K. (2017). Biomolecular condensates: Organizers of cellular biochemistry. *Nat. Rev. Mol. Cell Biol.* 18, 285–298. <https://doi.org/10.1038/nrm.2017.7>.
18. Shin, Y., and Brangwynne, C.P. (2017). Liquid phase condensation in cell physiology and disease. *Science* 357. eaaf43821126/science.aaf4382.
19. Hnisz, D., Shrinivas, K., Young, R.A., Chakraborty, A.K., and Sharp, P.A. (2017). A Phase Separation Model for Transcriptional Control. *Cell* 169, 13–23. <https://doi.org/10.1016/j.cell.2017.02.007>.

20. Boija, A., Klein, I.A., Sabari, B.R., Dall'Agnese, A., Coffey, E.L., Zamudio, A.V., Li, C.H., Shrinivas, K., Manteiga, J.C., Hannett, N.M., et al. (2018). Transcription Factors Activate Genes through the Phase-Separation Capacity of Their Activation Domains. *Cell* 175, 1842–1855.e16. <https://doi.org/10.1016/j.cell.2018.10.042>.
21. Basu, S., Mackowiak, S.D., Niskanen, H., Knezevic, D., Asimi, V., Grosswendt, S., Geertsma, H., Ali, S., Jerković, I., Ewers, H., et al. (2020). Un-blending of Transcriptional Condensates in Human Repeat Expansion Disease. *Cell* 181, 1062–1079.e30. <https://doi.org/10.1016/j.cell.2020.04.018>.
22. Morin, J.A., Wittmann, S., Choubey, S., Klosin, A., Golfier, S., Hyman, A.A., Jülicher, F., and Grill, S.W. (2022). Sequence-dependent surface condensation of a pioneer transcription factor on DNA. *Nat. Phys.* 18, 271–276. <https://doi.org/10.1038/s41567-021-01462-2>.
23. Trojanowski, J., Frank, L., Rademacher, A., Mücke, N., Grigaitis, P., and Rippe, K. (2022). Transcription activation is enhanced by multivalent interactions independent of phase separation. *Mol. Cell.* 82, 1878–1893.e10. <https://doi.org/10.1016/J.MOLCEL.2022.04.017>.
24. Trojanowski, J., and Rippe, K. (2022). Transcription factor binding and activity on chromatin. *Curr. Opin. Struct. Biol.* 31, 1004381016/J.COISB.2022.100438.
25. Li, J., Hsu, A., Hua, Y., Wang, G., Cheng, L., Ochiai, H., Yamamoto, T., and Pertsinidis, A. (2020). Single-gene imaging links genome topology, promoter–enhancer communication and transcription control. *Nat. Struct. Mol. Biol.* 27, 1032–1040. <https://doi.org/10.1038/s41594-020-0493-6>.
26. Erdel, F., and Rippe, K. (2018). Formation of Chromatin Subcompartments by Phase Separation. *Biophys. J.* 114, 2262–2270. <https://doi.org/10.1016/J.BPJ.2018.03.011>.
27. Pundhir, S., Bratt Lauridsen, F.K., Schuster, M.B., Jakobsen, J.S., Ge, Y., Schoof, E.M., Rapin, N., Waage, J., Hasemann, M.S., and Porse, B.T. (2018). Enhancer and Transcription Factor Dynamics during Myeloid Differentiation Reveal an Early Differentiation Block in Cebpa null Progenitors. *Cell Rep.* 23, 2744–2757. <https://doi.org/10.1016/j.celrep.2018.05.012>.
28. Avellino, R., and Delwel, R. (2017). Expression and regulation of C/EBP $\alpha$  in normal myelopoiesis and in malignant transformation. *Blood* 129, 2083–2091. <https://doi.org/10.1182/BLOOD-2016-09-687822>.
29. Wang, N.D., Finegold, M.J., Bradley, A., Ou, C.N., Abdelsayed, S., v., Wilde, M.D., Taylor, L.R., Wilson, D.R., and Darlington, G.J. (1995). Impaired energy homeostasis in C/EBP alpha knockout mice. *Science* 269, 1108–1112. <https://doi.org/10.1126/SCIENCE.7652557>.
30. Hasemann, M.S., Lauridsen, F.K.B., Waage, J., Jakobsen, J.S., Frank, A.K., Schuster, M.B., Rapin, N., Bagger, F.O., Hoppe, P.S., Schroeder, T., et al. (2014). C/EBP $\alpha$  is required for long-term self-renewal and lineage priming of hematopoietic stem cells and for the maintenance of epigenetic configurations in multipotent progenitors. *PLoS Genet.* 10. <https://doi.org/10.1371/JOURNAL.PGEN.1004079>.
31. Ye, M., Zhang, H., Amabile, G., Yang, H., Staber, P.B., Zhang, P., Levantini, E., Alberich-Jordà, M., Zhang, J., Kawasaki, A., et al. (2013). C/EBP $\alpha$  controls acquisition and maintenance of adult hematopoietic stem cell quiescence. *Nat. Cell Biol.* 15. <https://doi.org/10.1038/NCB2698>.
32. Nerlov, C., and Ziff, E.B. (1994). Three levels of functional interaction determine the activity of CCAAT/enhancer binding protein-alpha on the serum albumin promoter. *Genes Dev.* 8, 350–362. <https://doi.org/10.1101/GAD.8.3.350>.
33. Xie, H., Ye, M., Feng, R., and Graf, T. (2004). Stepwise reprogramming of B cells into macrophages. *Cell* 117, 663–676.
34. Rapino, F., Robles, E.F., Richter-Larrea, J.A., Kallin, E.M., Martinez-Cli-mont, J.A., and Graf, T. (2013). C/EBP $\alpha$  induces highly efficient macrophage transdifferentiation of B lymphoma and leukemia cell lines and impairs their tumorigenicity. *Cell Rep.* 3, 1153–1163. <https://doi.org/10.1016/j.celrep.2013.03.003>.
35. Stik, G., Vidal, E., Barrero, M., Cuartero, S., Vila-Casadesús, M., Men-diesta-Esteban, J., Tian, T.V., Choi, J., Berenguer, C., Abad, A., et al. (2020). CTCF is dispensable for immune cell transdifferentiation but facilitates an acute inflammatory response. *Nat. Genet.* 52, 655–661. <https://doi.org/10.1038/s41588-020-0643-0>.
36. Ahn, J.H., Davis, E.S., Daugird, T.A., Zhao, S., Quiroga, I.Y., Uryu, H., Li, J., Storey, A.J., Tsai, Y.H., Keeley, D.P., et al. (2021). Phase separation drives aberrant chromatin looping and cancer development. *Nature* 2021 595, 591–595. <https://doi.org/10.1038/s41586-021-03662-5>.
37. Martin, E.W., and Mittag, T. (2018). Relationship of Sequence and Phase Separation in Protein Low-Complexity Regions. *Biochemistry* 57, 2478–2487. [https://doi.org/10.1021/ACS.BIOCHEM.8B00008/ASSET/IMAGES/MEDIUM/B1-2018-00008N\\_0006.GIF](https://doi.org/10.1021/ACS.BIOCHEM.8B00008/ASSET/IMAGES/MEDIUM/B1-2018-00008N_0006.GIF).
38. Fang, X., Wang, L., Ishikawa, R., Li, Y., Fiedler, M., Liu, F., Calder, G., Rowan, B., Weigel, D., Li, P., and Dean, C. (2019). *Arabidopsis* FLL2 pro-motes liquid–liquid phase separation of polyadenylation complexes. *Nature* 2019 569, 265–269. <https://doi.org/10.1038/s41586-019-1165-8>.
39. Sharma, R., Choi, K.J., Quan, M.D., Sharma, S., Sankaran, B., Park, H., LaGrone, A., Kim, J.J., MacKenzie, K.R., Ferreon, A.C.M., et al. (2021). Liquid condensation of reprogramming factor KLF4 with DNA provides a mechanism for chromatin organization. *Nat. Commun.* 12, 5579–5617. <https://doi.org/10.1038/s41467-021-25761-7>.
40. Sabari, B.R., Dall'Agnese, A., Boija, A., Klein, I.A., Coffey, E.L., Shrinivas, K., Abraham, B.J., Hannett, N.M., Zamudio, A.V., Manteiga, J.C., et al. (2018). Coactivator condensation at super-enhancers links phase separation and gene control. *Science* 361, eaar3958. <https://doi.org/10.1126/science.aar3958>.
41. Heinz, S., Romanoski, C.E., Benner, C., Allison, K.A., Kaikkonen, M.U., Or-ozco, L.D., and Glass, C.K. (2013). Effect of natural genetic variation on enhancer selection and function. *Nature* 503, 487–492. <https://doi.org/10.1038/NATURE12615>.
42. van Oevelen, C., Collombet, S., Vicent, G., Hoogenkamp, M., Lepoivre, C., Badeaux, A., Bussmann, L., Sardina, J.L., Thieffry, D., Beatò, M., et al. (2015). C/EBP $\alpha$  Activates Pre-existing and De Novo Macrophage En-hancers during Induced Pre-B Cell Transdifferentiation and Myelopoiesis. *Stem Cell Rep.* 5, 232–247. <https://doi.org/10.1016/j.stemcr.2015.06.007>.
43. Rosen, E.D., Hsu, C.H., Wang, X., Sakai, S., Freeman, M.W., Gonzalez, F.J., and Spiegelman, B.M. (2002). C/EBP $\alpha$  induces adipogenesis through PPAR $\gamma$ : a unified pathway. *Genes Dev.* 16. <https://doi.org/10.1101/GAD.948702>.
44. Nechanitzky, R., Akbas, D., Scherer, S., Györy, I., Hoyler, T., Ramamoorthy, S., Diefenbach, A., and Grosschedl, R. (2013). Transcription factor EBF1 is essential for the maintenance of B cell identity and prevention of alternative fates in committed cells. *Nat. Immunol.* 14, 867–875. <https://doi.org/10.1038/NI.2641>.
45. Yoshida, T., Ng, S.Y.M., Zuniga-Pflucker, J.C., and Georgopoulos, K. (2006). Early hematopoietic lineage restrictions directed by Ikaros. *Nat. Immunol.* 7, 382–391. <https://doi.org/10.1038/NI1314>.
46. Staller, M.V., Holehouse, A.S., Swain-Lenz, D., Das, R.K., Pappu, R.V., Cohen, B.A., v., Holehouse, A.S., Swain-Lenz, D., Das, R.K., Pappu, R.v., and Cohen, B.A. (2018). A High-Throughput Mutational Scan of an Intrinsically Disordered Acidic Transcriptional Activation Domain. *Cell Syst.* 6, 444–455.e6. <https://doi.org/10.1016/j.CELS.2018.01.015/ATTACHMENT/E0A815EC-9F98-451B-8236-CEDC607E0AB3/MMC5.CSV>.
47. Basu, S., Martínez-Cristóbal, P., Pesarrodon, M., Frigolé-Vivas, M., Lewis, M., Szulc, E., Bañuelos, C.A., Sánchez-Zarzalejo, C., Bielskuté, S., Zhu, J., et al. (2022). Rational optimization of a transcription factor acti-vation domain inhibitor. Preprint at bioRxiv. <https://doi.org/10.1101/2022.08.18.504385>.
48. Vernon, R.M., Chong, P.A., Tsang, B., Kim, T.H., Bah, A., Farber, P., Lin, H., and Forman-Kay, J.D. (2018). Pi-Pi contacts are an overlooked protein feature relevant to phase separation. *Elife* 7, e31486. 7554/ELIFE.31486.

49. Wang, J., Choi, J.M., Holehouse, A.S., Lee, H.O., Zhang, X., Jahnel, M., Maharana, S., Lemaitre, R., Pozniakovsky, A., Drechsel, D., et al. (2018). A Molecular Grammar Governing the Driving Forces for Phase Separation of Prion-like RNA Binding Proteins. *Cell* 174, 688–699.e16. <https://doi.org/10.1016/J.CELL.2018.06.006>.
50. Pedersen, T.Å., Kowenz-Leutz, E., Leutz, A., and Nerlov, C. (2001). Cooperation between C/EBPalpha TBP/TFIIB and SWI/SNF recruiting domains is required for adipocyte differentiation. *Genes Dev.* 15, 3208–3216. <https://doi.org/10.1101/GAD.209901>.
51. Wang, F., He, J., Liu, S., Gao, A., Yang, L., Sun, G., Ding, W., Li, C.Y., Gou, F., He, M., et al. (2021). A comprehensive RNA editome reveals that edited Azin1 partners with DDX1 to enable hematopoietic stem cell differentiation. *Blood* 138, 1939–1952. <https://doi.org/10.1182/BLOOD.2021011314>.
52. Zhang, C., Xu, Z., Yang, S., Sun, G., Jia, L., Zheng, Z., Gu, Q., Tao, W., Cheng, T., Li, C., and Cheng, H. (2020). tagHi-C Reveals 3D Chromatin Architecture Dynamics during Mouse Hematopoiesis. *Cell Rep.* 32, 1082061016/j.celrep.2020.108206.
53. Plana-Carmona, M., Stik, G., Bulteau, R., Segura-Morales, C., Alcázar, N., Wyatt, C.D.R., Klonizakis, A., de Andrés-Aguayo, L., Gasnier, M., Tian, T.V., et al. (2022). The trophectoderm acts as a niche for the inner cell mass through C/EBP $\alpha$ -regulated IL-6 signaling. *Stem Cell Rep.* 17, 1991–2004. <https://doi.org/10.1016/J.STEMCR.2022.07.009>.
54. Uhlén, M., Fagerberg, L., Hallström, B.M., Lindskog, C., Oksvold, P., Marinoglu, A., Sivertsson, Å., Kampf, C., Sjöstedt, E., Asplund, A., et al. (2015). Tissue-based map of the human proteome. *Science* 347. [https://doi.org/10.1126/SCIENCE.1260419/SUPPL\\_FILE/1260419\\_UHLEN\\_SM.PDF](https://doi.org/10.1126/SCIENCE.1260419/SUPPL_FILE/1260419_UHLEN_SM.PDF).
55. Choi, J., Lysakovskaya, K., Stik, G., Demel, C., Söding, J., Tian, T.V., Graf, T., Cramer, P., v., Graf, T., and Cramer, P. (2021). Evidence for additive and synergistic action of Mammalian enhancers during cell fate determination. *Elife* 10. <https://doi.org/10.7554/eLife.65381>.
56. Erijman, A., Kozlowski, L., Sohrabi-Jahromi, S., Fishburn, J., Warfield, L., Schreiber, J., Noble, W.S., Söding, J., and Hahn, S. (2020). A High-Throughput Screen for Transcription Activation Domains Reveals Their Sequence Features and Permits Prediction by Deep Learning. *Mol. Cell.* 79, 1066–1062.e6. <https://doi.org/10.1016/J.MOLCEL.2020.04.020>.
57. Sanborn, A.L., Yeh, B.T., Feigerle, J.T., Hao, C.V., Townshend, R.J., Lieberman Aiden, E., Dror, R.O., and Kornberg, R.D. (2021). Simple biochemical features underlie transcriptional activation domain diversity and dynamic, fuzzy binding to mediator. *Elife* 10, e680687554. <https://doi.org/10.1101/ELIFE.68068>.
58. Staller, M.V., Holehouse, A.S., Swain-Lenz, D., Das, R.K., Pappu, R.V., and Cohen, B.A. (2018). A High-Throughput Mutational Scan of an Intrinsically Disordered Acidic Transcriptional Activation Domain. *Cell Syst.* 6, 444–455.e6. <https://doi.org/10.1016/J.CELLS.2018.01.015/ATTACHMENT/EOA815EC-9F98-451B-8236-CEDC607E0AB3/MMC5.CSV>.
59. Staller, M.V., Ramirez, E., Kotha, S.R., Holehouse, A.S., Pappu, R.V., and Cohen, B.A. (2022). Directed mutational scanning reveals a balance between acidic and hydrophobic residues in strong human activation domains. *Cell Syst.* 13, 334–345.e5. <https://doi.org/10.1016/J.CELLS.2022.01.002>.
60. Mittag, T., and Pappu, R.V. (2022). A conceptual framework for understanding phase separation and addressing open questions and challenges. *Mol. Cell.* 82, 2201–2214. <https://doi.org/10.1016/J.MOLCEL.2022.05.018>.
61. Chong, S., Dugast-Darzacq, C., Liu, Z., Dong, P., Dailey, G.M., Cattoglio, C., Heckert, A., Banala, S., Lavis, L., Darzacq, X., and Tjian, R. (2018). Imaging dynamic and selective low-complexity domain interactions that control gene transcription. *Science* 361. eaar25551126/science.aar2555.
62. McSwiggen, D.T., Hansen, A.S., Teves, S.S., Marie-Nelly, H., Hao, Y., Heckert, A.B., Umemoto, K.K., Dugast-Darzacq, C., Tjian, R., and Darzacq, X. (2019). Evidence for DNA-mediated nuclear compartmentalization distinct from phase separation. *Elife* 8, e470987554. <https://doi.org/10.1101/ELIFE.47098>.
63. Mir, M., Bickmore, W., Furlong, E.E.M., and Narlikar, G. (2019). Chromatin topology, condensates and gene regulation: shifting paradigms or just a phase? *Development* 146. <https://doi.org/10.1242/DEV.182766>.
64. Itoh, Y., Iida, S., Tamura, S., Nagashima, R., Shiraki, K., Goto, T., Hibino, K., Ide, S., and Maeshima, K. (2021). 1,6-hexanediol rapidly immobilizes and condenses chromatin in living human cells. *Life Sci. Alliance* 4, e20200100526508. <https://doi.org/10.1101/LSA.202001005/VIDEO-2>.
65. Düster, R., Kalthenauer, I.H., Schmitz, M., and Geyer, M. (2021). 1,6-Hexanediol, commonly used to dissolve liquid–liquid phase separated condensates, directly impairs kinase and phosphatase activities. *J. Biol. Chem.* 296, 100260–100261. <https://doi.org/10.1016/J.JBC.2021.100260>.
66. Liu, X., Jiang, S., Ma, L., Qu, J., Zhao, L., Zhu, X., and Ding, J. (2021). Time-dependent effect of 1,6-hexanediol on biomolecular condensates and 3D chromatin organization. *Genome Biol.* 22, 230–329. <https://doi.org/10.1186/S13059-021-02455-3/FIGURES/6>.
67. Jack, I., Seshadri, R., Garson, M., Michael, P., Callen, D., Zola, H., and Morley, A. (1986). RCH-ACV: A lymphoblastic leukemia cell line with chromosome translocation 1;19 and trisomy 8. *Cancer Genet. Cytogenet.* 19, 261–269. [https://doi.org/10.1016/0165-4608\(86\)90055-5](https://doi.org/10.1016/0165-4608(86)90055-5).
68. Ran, F.A., Hsu, P.D., Wright, J., Agarwala, V., Scott, D.A., and Zhang, F. (2013). Genome engineering using the CRISPR-Cas9 system. *Nat. Protoc.* 8, 2281–2308. <https://doi.org/10.1038/nprot.2013.143>.
69. Schindelin, J., Arganda-Carreras, I., Frise, E., Kaynig, V., Longair, M., Pietzsch, T., Reisert, S., Rueden, C., Saalfeld, S., Schmid, B., et al. (2012). Fiji: an open-source platform for biological-image analysis. *Nat. Methods* 9, 676–682. <https://doi.org/10.1038/nmeth.2019>.
70. Bolte, S., and Cordelières, F.P. (2006). A guided tour into subcellular co-localization analysis in light microscopy. *J. Microsc.* 224, 213–232. <https://doi.org/10.1111/j.1365-2818.2006.01706.X>.
71. MANDERS, E.M.M., VERBEEK, F.J., and ATEN, J.A. (1993). Measurement of co-localization of objects in dual-colour confocal images. *J. Microsc.* 169, 375–382. <https://doi.org/10.1111/j.1365-2818.1993.tb03313.x>.
72. Bates, M., Huang, B., Dempsey, G.T., and Zhuang, X. (2007). Multicolor super-resolution imaging with photo-switchable fluorescent probes. *Science* 317, 1749–1753. <https://doi.org/10.1126/SCIENCE.1146598>.
73. Rust, M.J., Bates, M., and Zhuang, X. (2006). Sub-diffraction-limit imaging by stochastic optical reconstruction microscopy (STORM). *Nat. Methods* 3, 793–795. <https://doi.org/10.1038/NMETH929>.
74. Ricci, M.A., Manzo, C., García-Parajo, M.F., Lakadamyali, M., and Cosma, M.P. (2015). Chromatin fibers are formed by heterogeneous groups of nucleosomes in vivo. *Cell* 160, 1145–1158. <https://doi.org/10.1016/J.CELL.2015.01.054>.
75. Neguembor, M.V., Martin, L., Castells-García, Á., Gómez-García, P.A., Vicario, C., Carnevali, D., AlHaj Abed, J., Granados, A., Sebastian-Perez, R., Sottili, F., et al. (2021). Transcription-mediated supercoiling regulates genome folding and loop formation. *Mol. Cell.* 81, 3065–3081.e12. <https://doi.org/10.1016/J.MOLCEL.2021.06.009>.
76. Emenecker, R.J., Griffith, D., and Holehouse, A.S. (2021). Metapredict: a fast, accurate, and easy-to-use predictor of consensus disorder and structure. *Biophys. J.* 120, 4312–4319. <https://doi.org/10.1016/J.BPJ.2021.08.039>.
77. Jumper, J., Evans, R., Pritzel, A., Green, T., Figurnov, M., Ronneberger, O., Tunyasuvunakool, K., Bates, R., Žídek, A., Potapenko, A., et al. (2021). Highly accurate protein structure prediction with AlphaFold. *Nature* 2021 596, 583–589. <https://doi.org/10.1038/s41586-021-03819-2>.
78. Alberti, S., Saha, S., Woodruff, J.B., Franzmann, T.M., Wang, J., and Hyman, A.A. (2018). A User's Guide for Phase Separation Assays with Purified Proteins. *J. Mol. Biol.* 430, 4806–4820. <https://doi.org/10.1016/J.JMB.2018.06.038>.
79. Soochit, W., Sleutels, F., Stik, G., Bartkuhn, M., Basu, S., Hernandez, S.C., Merzouk, S., Vidal, E., Boers, R., Boers, J., et al. (2021). CTCF chromatin residence time controls three-dimensional genome organization, gene

expression and DNA methylation in pluripotent cells. *Nat. Cell Biol.* 23, 881–893. <https://doi.org/10.1038/s41556-021-00722-w>.

80. Serra, F., Baù, D., Goodstadt, M., Castillo, D., Filion, G., and Marti-Renom, M.A. (2017). Automatic analysis and 3D-modelling of Hi-C data using TAD-bit reveals structural features of the fly chromatin colors. *PLoS Comput. Biol.* 13. <https://doi.org/10.1371/journal.pcbi.1005665>.

81. Vidal, E., le Dily, F., Quilez, J., Stadhouders, R., Cuartero, Y., Graf, T., Marti-Renom, M.A., Beato, M., and Filion, G.J. (2018). OneD: increasing reproducibility of Hi-C samples with abnormal karyotypes. *Nucleic Acids Res.* 46, e49. <https://doi.org/10.1093/nar/gky064>.

82. Rao, S.S.P., Huntley, M.H., Durand, N.C., Stamenova, E.K., Bochkov, I.D., Robinson, J.T., Sanborn, A.L., Machol, I., Omer, A.D., Lander, E.S., and Aiden, E.L. (2014). A 3D Map of the Human Genome at Kilobase Resolution Reveals Principles of Chromatin Looping. *Cell* 159, 1665–1680. <https://doi.org/10.1016/J.CELL.2014.11.021>.

83. Zheng, X., and Zheng, Y. (2018). CscoreTool: fast Hi-C compartment analysis at high resolution. *Bioinformatics* 34, 1568–1570. <https://doi.org/10.1093/BIOINFORMATICS/BTX802>.

84. Ramírez, F., Bhardwaj, V., Arrigoni, L., Lam, K.C., Grüning, B.A., Villavacas, J., Habermann, B., Akhtar, A., and Manke, T. (2018). High-resolution TADs reveal DNA sequences underlying genome organization in flies. *Nat. Commun.* 9. <https://doi.org/10.1038/s41467-017-02525-w>.

85. Heinz, S., Texari, L., Hayes, M.G.B., Urbanowski, M., Chang, M.W., Givarkas, N., Rialdi, A., White, K.M., Albrecht, R.A., Pache, L., et al. (2018). Transcription Elongation Can Affect Genome 3D Structure. *Cell* 174, 1522–1536.e22. <https://doi.org/10.1016/J.CELL.2018.07.047>.

86. Quinlan, A.R., and Hall, I.M. (2010). BEDTools: A flexible suite of utilities for comparing genomic features. *Bioinformatics* 26, 841–842. <https://doi.org/10.1093/bioinformatics/btq033>.

87. Dobin, A., Davis, C.A., Schlesinger, F., Drenkow, J., Zaleski, C., Jha, S., Batut, P., Chaisson, M., and Gingeras, T.R. (2013). STAR: Ultrafast universal RNA-seq aligner. *Bioinformatics* 29, 15–21. <https://doi.org/10.1093/bioinformatics/bts635>.

88. Love, M.I., Huber, W., and Anders, S. (2014). Moderated estimation of fold change and dispersion for RNA-seq data with DESeq2. *Genome Biol.* 15, 5501186/s13059-014-0550-8.

89. Langmead, B., and Salzberg, S.L. (2012). Fast gapped-read alignment with Bowtie 2. *Nat. Methods* 9, 357–359. <https://doi.org/10.1038/nmeth.1923>.

90. Li, H., Handsaker, B., Wysoker, A., Fennell, T., Ruan, J., Homer, N., Marth, G., Abecasis, G., and Durbin, R.; 1000 Genome Project Data Processing Subgroup (2009). The Sequence Alignment/Map format and SAMtools. *Bioinformatics* 25, 2078–2079. <https://doi.org/10.1093/bioinformatics/btp352>.

91. Ramírez, F., Dündar, F., Diehl, S., Grüning, B.A., and Manke, T. (2014). DeepTools: A flexible platform for exploring deep-sequencing data. *Nucleic Acids Res.* 42. <https://doi.org/10.1093/nar/gku365>.

92. Feng, J., Liu, T., Qin, B., Zhang, Y., and Liu, X.S. (2012). Identifying ChIP-seq enrichment using MACS. *Nat. Protoc.* 7, 1728–1740. <https://doi.org/10.1038/nprot.2012.101>.

93. McLean, C.Y., Bristor, D., Hiller, M., Clarke, S.L., Schaar, B.T., Lowe, C.B., Wenger, A.M., and Bejerano, G. (2010). GREAT improves functional interpretation of cis-regulatory regions. *Nat. Biotechnol.* 28, 495–501. <https://doi.org/10.1038/nbt.1630>.

94. Huang, B., Wang, W., Bates, M., and Zhuang, X. (2008). Three-dimensional super-resolution imaging by stochastic optical reconstruction microscopy. *Science* 319, 810–813. <https://doi.org/10.1126/SCIENCE.1153529>.

STAR★METHODS

KEY RESOURCES TABLE

REAGENT or RESOURCE	SOURCE	IDENTIFIER
<b>Antibodies</b>		
BRD4 rabbit monoclonal antibody	Abcam	Cat# 128874; RRID: AB_11145462
Polyclonal Rabbit anti-Human IKZF1/IKAROS Antibody	LSBio	LS-C331729
EBF1 rabbit polyclonal antibody	Abnova	H00001879-DOIP; RRID:AB_537882
C/EBP $\alpha$ (D56F10) XP <sup>®</sup> Rabbit monoclonal antibody	Cell Signaling	8178; RRID:AB_11178517
P300 monoclonal mouse antibody	Active Motif	RRID: AB_2716754
mouse monoclonal HP1 $\alpha$ antibody	Santa Cruz	sc-515341
mouse OCT4 monoclonal antibody	Santa Cruz	sc-5279;RRID:AB_628051
mouse SC-35 monoclonal antibody	Sigma	S4045;RRID:AB_477511
mouse monoclonal GFP antibody	Abcam	ab1218;RRID:AB_298911
Donkey anti-rabbit Alexa Fluor 555-coupled secondary antibody	Life Technologies	A-31572;RRID:AB_162543
Goat anti-mouse IgG Alexa Fluor 546	Life Technologies	A11018; RRID:AB_1500742
Goat anti-Rabbit IgG Alexa Fluor 647	Molecular Probes	A21245; RRID:AB_141775
Goat anti-rabbit IgG Alexa Fluor 488	Molecular Probes	A11070;RRID:AB_142134
Alexa Fluor 555 goat Anti-mouse IgG1	Life Technologies	A21127;RRID:AB_141596
AF647-CD34 rat anti-mouse	BD Biosciences	560230; RRID:AB_1645200
APC-eFluor780 CD117 (c-kit) rat anti-mouse	eBioscience	47-1171-80; RRID:AB_1272213
PE-Cy7 Ly-6A/E (Sca-1) rat anti-mouse	eBioscience	25-5981-81; RRID:AB_469668
BV711 Rat Anti-Mouse CD16/CD32	BD Biosciences	747947; RRID:AB_2872408
<b>Bacterial and virus strains</b>		
pHAGE-TetO-CEBPA-WT-mEGFP	This paper	N/A
pHAGE-TetO-CEBPA-AroLITE-mEGFP	This paper	N/A
<b>Critical commercial assays</b>		
NEBNext DNA Library prep kit	New England Biolabs	E6040
Dual-Glo Luciferase Assay system	Promega	E2920
Nucelofector <sup>®</sup> kit-C	Amaxa	VCA-1004
Lineage Cell Depletion Kit, mouse	Miltenyi Biotec	130-090-858
LS columns	Miltenyi Biotec	130-042-401
<b>Deposited data</b>		
Raw and Hi-C data generated from the KO B cells	This paper	GEO: GSE221167
Hi-C and RNA-seq from B cell transdifferentiation	Stik et al. <sup>35</sup>	GEO: GSE140528
CEBPA and BRD4 ChIP-seq datasets from B cell transdifferentiation	Stik et al. <sup>35</sup>	GEO: GSE131620
CEBPA ChIP-seq data of GMP cells	Hasemann et al. <sup>30</sup>	GEO: GSE43007
tag-HiC dataset datasets of hematopoietic cells	Zhang et al. <sup>52</sup>	GEO: GSE142216
RNA-seq datasets of hematopoietic cells	Wang et al. <sup>51</sup>	GEO: GSE152918
Hi-C of HepG2	ENCODE	ENCLB022KPF
CEBPA ChIP-seq HepG2	ENCODE	ENCSR142IGM
BRD4 ChIP-seq HepG2	ENCODE	ENCSR395MHA

(Continued on next page)

**Continued**

REAGENT or RESOURCE	SOURCE	IDENTIFIER
<b>Experimental models: Cell lines</b>		
BLaER1	Rapino et al. <sup>34</sup>	N/A
RCH-ACV	Cellosaurus	CVCL_1851
HepG2	ATCC	HB-8065
HEK293T	ATCC	CRL-3216
<b>Experimental models: Organisms/strains</b>		
Mouse B6CBAF1/Crl	The Jackson Laboratory	JAX: 100011
Mouse Med1-mEGFP	This paper	N/A
<b>Oligonucleotides</b>		
qPCR primers	<a href="#">Table S1</a>	N/A
<b>Recombinant DNA</b>		
pHAGE-CEBPA-WT-mEGFP	This paper	N/A
pHAGE-CEBPA-AroLITE-mEGFP	This paper	N/A
pX330_mCherry	Addgene	98750
pX459	Addgene	62988
pET-IDR-CEBPA-WT-mEGFP	This paper	N/A
pET-IDR-CEBPA-AroLITE-mEGFP	This paper	N/A
pET-ΔIDR-CEBPA-mEGFP	This paper	N/A
pET-CEBPA-FL	This paper	N/A
pET-PPARG-mCherry	This paper	N/A
pET-PU1-mCherry	This paper	N/A
pET-NPM1-mCherry	This paper	N/A
pET-MED1-IDR-mCherry	Sabari et al. <sup>27</sup>	N/A
pET-MED1-IDR-EBFP2	This paper	N/A
<b>Software and algorithms</b>		
ImageJ	Schneider et al.	<a href="https://ImageJ.nih.gov/ij/">https://ImageJ.nih.gov/ij/</a>
STAR	Dobin et al.	<a href="https://github.com/alexdobin/STAR">https://github.com/alexdobin/STAR</a>
HiC explorer	Ramirez et al.	<a href="https://hicexplorer.readthedocs.io/en/latest/">https://hicexplorer.readthedocs.io/en/latest/</a>
Homer	Heinz et al.	<a href="http://homer.ucsd.edu/homer/index.html">http://homer.ucsd.edu/homer/index.html</a>
Cscore Tool	Zheng et al.	<a href="https://github.com/scoutzbx/CscoreTool">https://github.com/scoutzbx/CscoreTool</a>
BedTools	Quinlan et al.	<a href="https://bedtools.readthedocs.io/en/latest/">https://bedtools.readthedocs.io/en/latest/</a>
Bowtie2	Langmead and Salzberg	<a href="http://bowtie-bio.sourceforge.net/bowtie2/index.shtml">http://bowtie-bio.sourceforge.net/bowtie2/index.shtml</a>
deepTools	Ramirez et al.	<a href="https://deeptools.readthedocs.io/en/latest/">https://deeptools.readthedocs.io/en/latest/</a>
Tadbit	Serra et al.	<a href="https://3dgenomes.github.io/TADbit/">https://3dgenomes.github.io/TADbit/</a>
MATLAB	MathWorks	<a href="https://www.mathworks.com/products/matlab.html">https://www.mathworks.com/products/matlab.html</a>
DESeq2	Love et al.	<a href="https://bioconductor.org/packages/DESeq2/">https://bioconductor.org/packages/DESeq2/</a>
SAMtools	Li et al.	<a href="http://samtools.sourceforge.net/">http://samtools.sourceforge.net/</a>
MACS2	Feng et al.	<a href="https://hbctraining.github.io/Intro-to-ChIPseq/lessons/05_peak_calling_macs.html">https://hbctraining.github.io/Intro-to-ChIPseq/lessons/05_peak_calling_macs.html</a>
Insight3	Huang et al.	<a href="http://huanglab.ucsf.edu/Resources.html">http://huanglab.ucsf.edu/Resources.html</a>
GREAT	McLean et al.	<a href="http://great.stanford.edu/public/html/">http://great.stanford.edu/public/html/</a>

**RESOURCE AVAILABILITY**

**Lead contact**

Further information and request for reagents and resources should be directed to and will be fulfilled by the lead contact, Grégoire Stik (Email: [gstik@carrerasresearch.org](mailto:gstik@carrerasresearch.org))

**Materials availability**

This study did not generate new unique reagents. All plasmids and cell lines generated in this study are available from the [lead contact](#) with a completed Materials Transfer Agreement as applicable.

**Data and code availability**

- Hi-C and RNA-seq dataset during B cell to macrophage transdifferentiation are publicly available in the Gene Expression Omnibus under accession number GSE140528. CEBPA and BRD4 ChIP-seq datasets under accession number GSE131620. tag-HiC dataset and RNA-seq datasets of hematopoietic cells are available under accession numbers GSE142216 and GSE152918, respectively. CEBPA ChIP-seq data of GMP cells are available in the Gene Expression Omnibus under accession number GSE43007. HiC, CEBPA and BRD4 ChIP-seq datasets of HepG2 cells are available in Encode under accession numbers ENCODE:ENCLB022KPF, ENCODE:ENCSR142IGM and ENCODE:ENCSR395MHA, respectively. Hi-C datasets generated at 0h and 24h during transdifferentiation of B cells KO for the CEBPA binding site are available under accession number GSE221167.
- This paper does report original code.
- Any additional information required to reanalyze the data reported in this work paper is available from the [lead contact](#) upon request.

**EXPERIMENTAL MODEL AND STUDY PARTICIPANT DETAILS****Cell culture**

HEK293T and HepG2 cells were cultured in knockout DMEM (Gibco) containing 10% fetal bovine serum, supplemented with 1% glutamine (Gibco), 1% penicillin/streptomycin (Thermo). Cells were split at 80–90% confluence. Medium was changed every 2–3 days.

RCH-rtTA and BLaER cells were derived from the RCH-ACV lymphoblastic leukemia cell line.<sup>67</sup> BLaER, RCH-rtTA cells and derivatives were cultured in RPMI (Gibco) containing 10% FBS, supplemented with 1% glutamine (Gibco), 1% penicillin/streptomycin (Thermo) and 550 µM β-mercaptoethanol (Gibco). Cells were maintained at a density of 0.1–6x10<sup>6</sup> cells/mL. Cells were checked for mycoplasma contamination every month and tested negative. If not stated differently, all cells were cultured under standard conditions at 37°C and 5% CO<sub>2</sub>.

**Mice models**

B6CBAF1/Crl mice (females from 6 to 12 week-old and male from 10 to 52 week-old) were used for embryo culture (see Method details section). For GMPs extraction, we used newly established transgenic mice (2 females, 38- and 41-week-old) expressing endogenous MED1 tagged with GFP.

The mice were housed in standard cages under 12-h light–dark cycles and fed *ad libitum* with a standard chow diet. All experiments were approved by the Ethics Committee of the Barcelona Biomedical Research Park (PRBB) and performed according to Spanish and European legislation.

**METHOD DETAILS****Mouse embryo culture**

B6CBAF1/Crl females (purchased from Charles River laboratories) were super-ovulated by injecting pregnant mare's serum gonadotropin (100 µL of 50UI/mL PMSG, Foligon) followed by human chorionic gonadotropin (100 µL of 5UI/mL hCG, Veterin Corion) after 48 h. Females were then mated with B6CBAF1/Crl males and zygotes harvested from swollen ampullas 20 h after hCG injection. Cumulus cells were removed by incubation with 300 µg/mL hyaluronidase (H4272, Sigma) in M2 medium (M7167, Sigma). After washing the zygotes in a few drops of KSOM medium (MR-106-D, Millipore), they were cultured in KSOM microdrops under mineral oil (NO-400K, Nidacon) in an incubator with 5% CO<sub>2</sub> at 37°C. Embryos were handled with a mouth aspirator (A5177-5EA, Sigma) coupled to fire-polished glass Pasteur pipettes and collected at the blastocyst stage for protein immunostaining.

**Obtaining primary GMPs**

GMP cells were isolated from a newly established transgenic mouse (to be described) expressing endogenous MED1 tagged with GFP. Lin-c-Kit<sup>+</sup> Sca-1<sup>-</sup> CD16<sup>+</sup>/CD32<sup>+</sup> CD34<sup>+</sup> GMP cells were isolated from bone marrow by FACS sorting using a BD INFLUX sorting machine.

**Generation of doxycycline-inducible CEBPA overexpression lines in RCH cells**

First, RCH-rtTA cell line stably expressing reverse tetracycline-controlled transactivator was generated by viral infection with pHAGE2-EF1aFull-rtTA-IRES-Puro and clonal selection under puromycin (1 µg mL<sup>-1</sup>). TetO-CEBPA-WT-mEGFP and TetO-CEBPA-AroLITE-mEGFP plasmids were cloned via Gibson assembly using a pHAGE2-tetO backbone. HEK293T cells were

co-transfected with vector plasmid and packaging plasmid using calcium phosphate transfection. Viral supernatants were collected 48h later and concentrated by ultracentrifugation at 20,000g for 2h at 20°C. Viral concentrates were resuspended in PBS. RCH-ACV-rTA cells were transduced by centrifugation with concentrated virus solution for 2h at 32°C and 1,000g in culturing medium.

#### Generation of DNA constructs for transactivation assays

To study transactivation strength of CEBPA IDRs we amplified sequences from codon optimized gene fragments (Twist Bioscience) for CEBPA WT and AroLITE with specific primers. Amplified gene fragments were cloned into a pGAL4 (Addgene #145245) backbone, linearized with AsiSI (NEB) and BsiWI (NEB) via NEBuilder HiFi Assembly.

#### Transactivation assay

The transactivation strength of transcription factor IDRs was assayed using the Dual-Glo Luciferase Assay system (Promega). HEK293T stem cells were seeded on gelatin pre-coated 24-well plates with a density of  $1 \times 10^5$  cells per  $\text{cm}^2$ . After 24 h, every well was transfected with 200 ng pGal4 empty vector control or the equimolar amount of the expression construct carrying an IDR of interest, 250 ng of the *Firefly* luciferase expression vector (Promega) and 15 ng of the *Renilla* luciferase expression vector (Promega) using FuGENE HD transfection reagent (Promega) following the manufacturer's instructions. After 24 h, cells were washed once with PBS and lysed in 100  $\mu\text{L}$  of 1x Lysis Passive Buffer (Promega) for 15 min on a shaker at room temperature. Subsequently, 10  $\mu\text{L}$  of cell lysate was pipetted onto a white bottom 96-microwell plate in triplicates followed by quantification of *Firefly* and *Renilla* using the Dual-Glo Luciferase Assay System Quick Protocol for 96-well plates (Promega). Triplicate data was normalized to *Renilla* luminescence of the respective well and finally normalized to the empty vector control. Data are shown as mean  $\pm$  SD. All data shown were generated of 4 independent transfections from at least two cell passages (Figure S3E). All data were plotted with GraphPad PRISM9. To assess statistical significance, two-tailed t-tests were performed.

#### CRISPR-Cas9 genome editing

For genome editing in CEBPA inducible BLAER cells, we employed a previously published CRISPR/Cas9 method.<sup>68</sup> First, gRNAs specific for upstream and downstream regions of *CEBPA* binding site were designed using Custom Alt-R CRISPR-Cas9 guide RNA software (IDT) and cloned into pX330\_mCherry and pX459 vectors, respectively. We tested 3 upstream and 3 downstream gRNAs and selected the two most efficient gRNAs for subsequent experiments (gRNAs sequence available upon request). Then, for each reaction, 3 million cells were used to perform double nucleofection (Amaxa Nucleofector, Kit C, VCA-1004) with 2  $\mu\text{g}$  of pX330\_mCherry and pX459 gRNA vectors. On the following day, cells were treated with puromycin (1  $\mu\text{g mL}^{-1}$ ) and single cell sorting (BD Influx Cell Sorter) was performed 4 days after transfection to select alive mCherry positive cells. After sufficient recovery time and colony growth of the single cells, a mirror plate was generated and genomic DNA (according to Alt-R Genome Edition Detection Kit, IDT, 1075932) and the targeted locus analyzed by PCR to check for homozygous knockouts. Fragments from potential homozygous KO clones were validated by sequencing (GATC).

#### RNA extraction and quantitative RT-PCR

RNA was extracted with the RNeasy mini kit (Qiagen) and quantified with a NanoDrop spectrophotometer. cDNA was produced with a High-Capacity RNA-to-cDNA kit (Applied Biosystems) and was used for qRT-PCR analysis in triplicate reactions with SYBR Green QPCR Master Mix (Applied Biosystems). Primers are available in Table S1.

#### Live cell imaging

For live cell imaging, cells were grown on polylysine-coated plates and stained with Hoechst (1  $\mu\text{g mL}^{-1}$ ) for 30 min before imaging. Image acquisition was performed using the 63x/1.4 oil objective of the Leica SP5 Inverted Confocal microscope (Leica, Germany). We took images of different planes of the cells at a distance of approximately 800 nm and used the maximum projection of those images to (i) count the total number of CEBPA accumulations and (ii) measure the mean fluorescence intensity per cell. The number of accumulations was plotted against the mean fluorescence intensity per cell using R software.

#### Fluorescence Recovery After Photo bleaching (FRAP)

Two -three images were taken prior to photobleaching. The photobleaching itself consisted of 3 iterations using 488 nm light at 50% laser power. Fluorescence recovery was measured over time up to 81 s. After the background intensities were subtracted from the absolute fluorescence values, values were calculated relative to pre-bleaching time points. Quantifications are based on 4 to 12 FRAP experiments and the figure have been generated using R software. In order to avoid movement of the TetO-CEBPA-mEGFP transduced RCH-rTA cells upon laser exposure, the cells were plated in semi-solid methylcellulose-based medium supplemented with 2  $\mu\text{g mL}^{-1}$  doxycycline.

#### Immunostaining of RCH-ACV, HepG2, mouse embryos, primary GMP cells

TetO-CEBPA-mEGFP RCH-ACV cells were grown on polylysine-treated coverslips and induced 24h before fixation. The cells were centrifuged at 300g for 5 min to allow better attachment onto the coverslips and fixed in 4% PFA for 15 min. Cells were blocked and permeabilized in blocking buffer: 1x PBS, 0.5% BSA (9048-46-8, Sigma), 0.3% Triton X-100 (Sigma) for 20 min and incubated with

the primary antibodies for 20 min at RT. The following antibodies were used: BRD4 (rabbit Abcam 128874, 1/50), IKAROS (Lb-Biosc, LS-C331729, 1/100), EBF1 (abnova H00001879-DOIP, 1/50). Next, we washed three times with 0.5% Triton X-100 PBS (PBST) and incubated with a Donkey anti-rabbit Alexa Fluor 555-coupled secondary antibody (Life Technologies, A-31572, 1/1000) for 1 h at RT. Cells were washed three times in PBST and counterstained with Hoechst. Images were acquired using a Leica SP8 confocal microscope (Leica, Germany) and processed with ImageJ.

HepG2 cells were seeded at a density of  $2 \times 10^4$  cells.cm<sup>-1</sup> onto polylysine-treated coverslips. After 24 h, cells were washed twice with PBS and fixed with 4% PFA for 10 min at room temperature. The fixed cells were washed twice in PBS and permeabilized in 1x PBS, 0.5% Triton X-100 for 20 min at RT. Subsequently, cells were blocked in 1x PBS, 0.05% Triton X-100, 5% BSA for 1 h at RT. Incubation with the primary antibodies (rabbit CEBPA 1/100, Cell Signaling 8178, mouse P300 1/200 Active Motif AB\_2716754 or mouse HP1a 1/200 Santa Cruz sc-515341) in antibody buffer (1x PBS, 0.05% Triton X-100 + 1% BSA) was performed overnight at 4°C. The next morning, cells were gently washed twice with PBST and incubated with secondary antibody (goat anti-mouse IgG Alexa Fluor 546 1/1000 Life Technologies A11018, Goat anti-Rabbit IgG Alexa Fluor 647, Molecular Probes A21245, 1/1000) in antibody buffer for 1 h at RT. Cells were washed three times in PBST and mounted with VECTASHIELD Antifade Mounting Medium with DAPI (Vectorlabs H-1200-10). Images were acquired with a Zeiss LSM980 confocal microscope equipped with Airyscan.

E4.5 blastocysts were collected and fixed in 4% PFA for 10 min at room temperature after 4 days of *in vitro* culture. They were then washed twice in PBS for 5 min before permeabilization with 0.5% PBST for 15 min. Blastocysts were washed twice in 0.1% PBST for 5 min before incubation in 0.1% PBST containing 3% BSA for 45 min at RT. Embryos were then treated with primary antibodies (rabbit CEBPA 1/100 Cell Signaling 8178, mouse OCT4 1:100, Santa Cruz 5279 or mouse SC-35 Sigma S4045) diluted in 0.1% PBST containing 1% BSA overnight at 4°C inside a moistened chamber. Next morning, embryos were sequentially washed in 0.1% PBST for 5, 15, 20 and 30 min at RT. A second blocking was performed in 0.1% PBST containing 3% BSA for 45 min at RT, then blastocysts were placed in 0.1% PBST containing 1% BSA with secondary antibodies (goat anti-rabbit IgG Alexa Fluor 488 Molecular Probes A211070 and Alexa Fluor 555 goat Anti-mouse IgG1 Life Technologies A21127 both at 1/1000) and DAPI (D1306 Invitrogen 5 µg/mL) for 90 min at RT inside a moist, dark chamber. Three washes in 0.1% PBST were performed before mounting the blastocysts in 10 µL drops of PBS on 35 mm coverglass plates (P35G-1.0-14-C, MatTek) covered in light oil (M5310, Sigma). Of note, all the incubation steps were performed on shaking platforms. Embryos were imaged with a Zeiss LSM 980 with Airyscan 2 inverted confocal microscope and further processed in Fiji software.<sup>69</sup>

GMP cells were collected in a 24-well plate containing polylysine-treated coverslips, centrifuged at 300g for 5 min to allow better attachment and fixed in 4% PFA for 15 min. Immunostaining was performed as for HepG2 cells using primary antibodies mouse GFP (Abcam ab1218, 1/100), rabbit CEBPA (Cell Signaling 8178, 1/100), rabbit BRD4 (Abcam 128874, 1/50) and mouse HP1a (Santa Cruz sc-515341 1/200). Images were acquired using a Zeiss LSM980 Airyscan microscope and processed with FIJI.

### Airyscan imaging

Immunostained HepG2 cells, mouse blastocysts and GMPs were imaged by Airyscan super resolution microscopy using a ZEISS LSM 980 equipped with Airyscan 2. Cells were selected through routine confocal scanning and Airyscan parameters defined through ZEN 3.3 Smart Setup and optimized for each channel (405, 488, 555) using continuous mode. Master gain and laser power were adjusted to minimize saturation and 2X averaging was used to improve signal to noise ratio (SNR). Pixel reassignment and Deconvolution (Weiner filtering) were performed with ZEN Airyscan Processing. Automatic deconvolution settings were applied (calculated based on image SNR) and filter strength was fine-tuned individually for each channel.

### Co-localization analysis

For induced RCH and HepG2 and GMP super resolution images, cell nuclei were defined based on DAPI staining and an individual intensity threshold was applied for each channel to extract local maxima. A binary image of the same size as the maxima was created using ImageJ. After two binary images per cell were obtained, the Just Another Colocalization Plugin (JACoP) for ImageJ<sup>70</sup> was used and the Manders overlap coefficients was calculated.<sup>71</sup>

### Cell preparation and Immunolabeling for Stochastic Optical Reconstruction Microscopy (STORM) imaging

For STORM imaging, 24h-induced BLER cells were plated in borosilicate glass bottom 8-well chambers (Nunc Lab-Tek, #155411). Cells were fixed with PFA 4% (Alfa Aesar, #43368) for 10 min at room temperature (RT) and rinsed three times with PBS for 5 min each. Fixed cells were permeabilized in 0.3% Triton X-100 (Sigma-Aldrich) in PBS for 10 min at RT and then incubated in blocking buffer (10% BSA – 0.01% Triton X-100 in PBS) for 15 min at room temperature. Next, cells were incubated with anti-CEBPA primary antibody (HPA067937, Sigma) in blocking buffer at 1:50 dilution overnight at 4C. Cells were washed three times for 5 min each with wash buffer (2% BSA – 0.01% Triton X-100 in PBS), and incubated with a home-made<sup>72</sup> dye pair labeled secondary antibody (AF405-AF647-anti-rabbit) at a 1:50 dilution in blocking buffer for 45 min at RT. To label DNA, cells were incubated with PicoGreen (Thermo Fisher, #P7581) in PBS at 1:10000 dilution and then washed three times for 5 min each with wash buffer.

### STORM imaging

STORM was performed on an N-STORM 4.0 microscope (Nikon) equipped with a CFI HP Apochromat TIRF 100x 1.49 oil objective and an iXon Ultra 897 camera (Andor) and with Highly Inclined and Laminated Optical sheet illumination (HILO). Before every STORM

image acquisition, diffraction-limited images were taken for the chosen nuclei to capture the signal of DNA (PicoGreen), and CEBPA (AF647). Next, STORM imaging of CEBPA was performed in continuous acquisition mode with 10 ms exposure time for 60000 frames. 647 nm laser was used at constant  $\sim 2$  kW/cm<sup>2</sup> power density and 405 nm laser power was gradually increased over the imaging. Imaging buffer composition for STORM imaging was 100 mM Cysteamine MEA (Sigma-Aldrich, #30070) - 5% Glucose (Sigma-Aldrich, #G8270) - 1% Glox Solution (0.5 mg/mL glucose oxidase, 40 mg/mL catalase (Sigma-Aldrich, #G2133 and #C100)) in PBS.

### STORM imaging analysis

STORM images were analyzed and rendered in Insight3 (kind gift of Bo Huang, UCSF) as previously described.<sup>72,73</sup> Localizations were identified based on a threshold and fit to a simple Gaussian to determine the x and y positions. Localizations belonging to nuclei were selected using Fiji where nuclear masks were generated based on the DNA signal. Nuclear localizations of CEBPA were analyzed to identify cluster. Cluster analysis was performed as previously described.<sup>74,75</sup>

### Identification of intrinsically disordered protein regions

Intrinsically disordered protein regions (IDRs) were predicted using Metapredict V2<sup>76</sup> incorporating information from AlphaFold 2<sup>77</sup> at default settings (Figure 2A).

### Generation of DNA constructs for protein purification

Expression vectors were generated by cloning cDNA of CEBPA, PPAR $\gamma$  and PU.1 into the pETM14 expression plasmid. Sequences were cloned N-terminally to the fluorescence tag. The amplified gene fragment for NPM1 was cloned into a pET45-mEGFP backbone, linearized by restriction digest with Ascl (NEB) and HindIII (NEB). Sequences were cloned C-terminally to the fluorescence marker. The plasmid for MED1-mCherry expression was kindly provided by the lab of Rick Young (RY8686). This template was used to produce MED1-EBFP2. Primers are available upon request.

### Protein purification

Recombinant proteins were overexpressed in BL21 (DE3) in autoinduction media. *E. coli* pellets were resuspended in ice-cold Buffer A (50 mM Tris pH 7.5, 500 mM NaCl, 20 mM Imidazole) supplemented with cOmplete protease inhibitors (Sigma, 11697498001), 0.5% Triton X-100, 10% glycerol, 2mM DTT and 1mM PMSF. French press was performed and the lysate centrifuged 30000g for 30 min at 4°C. Protein purification was performed using Cytiva HisTrap HP Ni<sup>2+</sup> columns followed by Hitrap Q cation exchange. For the FL protein, an additional MBP column was used to remove the cleaved tag, followed by a size exclusion chromatography purification step. Eluted fractions were analyzed by SDS-PAGE (Figure S5) and fractions of interest pooled and concentrated. The concentrated fraction was diluted in Storage Buffer to give final concentrations of 50 mM Tris pH 7.5, 125 mM NaCl, 1 mM DTT, 10% Glycerol. Proteins were stored at -80°C.

### In vitro droplet assays

The purified mCherry-, mEGFP- or EBFP2- fusion proteins were measured for concentration, diluted to the desired concentration in Storage Buffer (50 mM Tris pH 7.5, 125 mM NaCl, 1 mM DTT, 10% Glycerol), and lastly PEG 4000 or Ficoll was added to the mix giving the following final concentrations in 5  $\mu$ L: 10  $\mu$ M total protein, 125 mM NaCl, 10% PEG unless otherwise stated. The mix was prepared on ice and then 2  $\mu$ L were loaded into a homemade sealed chamber slide comprising a glass coverslip (Deckgläser cover glasses #0101030) and double-sided tape (3M 300 LSE high-temperature double-sided tape of 0.17 mm thickness) shortly before imaging. Images were acquired using a Leica TCS SP8 confocal (HC PL APO 63x/1.40 OIL CS2 objective). Images were analyzed using an in-house ImageJ script to detect droplet regions, using mean intensity threshold of 3 standard deviations above the background intensity. To quantify PS of CEBPA with increasing protein concentration, we quantified the total area within defined droplet regions for 3-8 images per protein concentration. To quantify the co-phase separation of CEBPA-mEGFP WT and AroLITE with PU1-mCherry, droplet regions were defined in the mCherry channel and the mean intensities measured across both channels for mCherry and mEGFP. Figures were generated using Prism Graphpad 9. Controls images of the co-phase separation assays showing each protein alone at the same conditions are presented in Figure S6.

For the salt and temperature-dependent experiments, CEBPA-IDR WT or AroLITE protein was prepared in a buffer containing 50 mM Tris-HCl, 1 mM DTT, pH 7.5. Samples were prepared containing 10  $\mu$ M protein, the indicated NaCl concentrations, and 10% PEG 4000 in the same buffer. For imaging, 1.5  $\mu$ L of sample was deposited in a sealed chamber comprising a slide and a cover-slip sandwiching double-sided tape (3M 300 LSE high-temperature double-sided tape of 0.17 mm thickness). The used coverslips were previously coated with PEG-silane following the published protocol in.<sup>78</sup> Confocal fluorescence microscopy images were taken using a Zeiss LSM780 confocal microscope system with a Plan ApoChromat 63x 1.4 oil objective. Images were quantified using 3 images per condition and average droplet size was calculated for each condition. The same setup was used to image CEBPA FL (labeled with DyLight 488 dye - ThermoFisher Scientific), CEBPA-IDR-mEGFP, and CEBPA- $\Delta$ IDR-mEGFP in Figure 2B.

**Partitioning of CEBPA into MED1 IDR droplets**

MED1 solution was mixed and then diluted 1:1 with 20% PEG-8000 in de-ionized water (w/v). After 20 min of incubation at room temperature, we added the indicated concentration of the protein of interest and pipetted 10  $\mu$ L of this mix onto a chambered coverslip (Ibidi, 80826-90). Images were acquired using an LSM880 confocal microscope equipped with a Plan-Apochromat-63x/1.40 oil DIC objective. Data was acquired from at least 5 images of two independent image series per condition. We used the ZEN blue 3.1 Image Analysis and Intellesis software packages for the detection of droplet regions. Image segmentation was achieved by use of a previously trained ZEN Intellesis algorithm for classification of each individual pixel into foreground (droplet area) or background (image background). Generated probability maps with a minimal confidence of at least 90%, a minimum area of 3 pixels and watershed for primary objects were implemented into the ZEN Image Analysis module to classify regions of interest. Enrichment of protein in droplets was calculated by background subtraction from the mean intensity values of droplet areas in the respective channel. Figures were generated using RStudio.

**Protein sequences****CEBPA full length**

MESADFYVEPRPPMSSHLQSPPHAPSNAAFGPRGAGPAPPPAPPAAPEPLGGICEHETSIDISAYIDPAAFNDEFLADLFQHSRQQ  
EKAKAAAGPAGGGGDFDYPGAPAGPGGAVMSAGAHGPPPGYGCAGYLDGRLEPLYERVGAPALRPLVIKQEPREEDEAKQLALAG  
LFPYQPPPPPPPHPHASPAHLAQFQIAHCGQTTMHLQPGHPTPPPTPVPSHAAPALGAAGLPGPGSALKGLAGAHPDLRTGG  
GGGGSGAGAGKAKKSVDKNSNEYRVRRERNNIAVRKSRDAKQRNVETQQKVLELTSNDRLRKVEQLSRELDTLRGIFRQLPESSL  
VKAMGNCA

**CEBPA-IDR wild type**

MESADFYVEPRPPMSSHLQSPPHAPSNAAFGPRGAGPAPPPAPPAAPEPLGGICEHETSIDISAYIDPAAFNDEFLADLFQHSRQQ  
EKAKAAAGPAGGGGDFDYPGAPAGPGGAVMSAGAHGPPPGYGCAGYLDGRLEPLYERVGAPALRPLVIKQEPREEDEAKQLALAG  
LFPYQPPPPPPPHPHASPAHLAQFQIAHCGQTTMHLQPGHPTPPPTPVPSHAAPALGAAGLPGPGSALKGLAGA

CEBPA-IDR AroLITE MRGRGRAGSPGGRRRPAQAGGRRGSPCRENSNSPMESADAAEAEPRPPMSSHLQSPPHAPSSAAAGAP  
RGAGPAQPPAPPAPEPLGGICEHETSIDISAAIDPAAAANDEALADLAQHSRQQEKAAGVPTGGGGGDADAPGAPAGPGGAVMPG  
GAHGPPPGAGCAAAGALDGRLEPLAERVGAPALRPLVIKQEPREEDEAKQLALAGLAPAQPPPPPPSHPHPPPAHLAAPHLQAI  
AHCQ.

**CEBPA-ΔIDR**

HPDLRTGGGGGGAGAGKAKKSVDKNSNEYRVRRERNNIAVRKSRDAKQRNVETQQKVLELTSNDRLRKVEQLSRELDTLRGIFRQLPESSLVKAMGNCA

**MED1-IDR**

EHHSGSQGPLTTGDLGKEKTQKRVKEGNGTSNSTSGPGLDKPGKRSRTPSNDGSKDKPPRKKADTEGKSPSHSSSNRPFTPP  
STGGSKSPGSAGRSQTPPGVATPPIPKITIQPKGTVMVGPSSHSQYTSVSSGSKSHHSHSSSSSASTSGKMKSSKSEGSS  
SSKLSSSMYSSQGSSQSKNNSQSGKGPGSSPITKHGLSSGSSSTKMKPQGKPSSLNPSLSKPNISPSHSRPPGGSDKLASPM  
KPVPGTPPSSKAKSPISSGGGSHMSGTSSSGMKSQKTPPSSNSCTASSSFSSGSSMSSSQNHGSSKGKSP  
SRNKKPSLTAVIDKLKHGVVTSGPGGEDPLDQMVGTVNSTSSHPMSSKHNMSGGEFQGKREKSDKDKSKVSTGSSVDSSKKTSESK  
NVGSTGVAKIISKHDGGSPSIKAKVTLQKPGESSGEGLRPQMASSKNYGSPLISGSTPKHERGSPSHSKSPAYTPQNLDSSES  
EKSYQNSPSSDDGIRPLPEYSTEKHKKHKKEKKVKDKDRDRDKDRDKKSHSIKPESWSKSPISSDQSLSMSNTILSADRPSRLSP  
DFMIGEEDDD.

**PU.1**

MLQACKMEGFSLTAPPSDDLVTYDSELYQRPMDYYSFVGSDGESHSWDFSAHHVNNEFENFPENHTELQSVQPPQLQQLY  
RHMELEQMHVLDTMVPPHTGLSHQVSYMPRMCFFYQTLSPAHQQSSDEEEGERQSPPLEVSDGEADGLEPGPGLLHGETGSKKKI  
RLYQFLLDLLRSGDMKDSIWVVDKDKGTQFQSSKHEALAHRWGQKGNRKKMTYQKMARALRNYGKTGEVKKVKKLTYQFSGEVL  
GRGGLAERRLPPH.

**PPARG**

MGETLGDSPVDPHEGAFADALPMSTSQEITMVDTEMPFWPTNFGISSVDSLVMEDHSHSFDIKPFTTVDFSSISAPHYEDIPFTRADPMV  
ADYKYDQLQEQYQSAIKVEPASPPYYSEKTQLYNRPRHEEPSNSLMAIECRVCGDKASGFHYGVACEGCKGFFRTIRLKLIDRCNLN  
CRIHKKSRNKCQYCRFKCLAVGMSHNAIRFGRMPQAEKEKLLAEISSDIDQLNPESADLRLAKHLYDSYIKSFPLTKAKARAILTGKTT  
DKSPFVYDMNSLMMGEDKIKFKHITPLQEKSKEVAIRFQGQCQFRSVEAQETEYAKNIPGFINLDLNDQVTLLKGVHEIYTMLASLMN  
KDGVLISEGQGFMTREFLKSRLKPGDFMEPKFEFAVKFNALELDDSDLAIFIAVIILSGDRPGLLNVKPIEDIQDNLLQALELQLKLNHPES  
SQLFAKVLQKMTDLRQIVTEHVQLLVIKKTETDMSLHPLLQEYKDLY.

**NPM1**

MEDSMMDMSPLRPQNYLFGCELKADKDYHFKVDNDENEHQLSLRTVSLGAGAKDELHIVEAEAMNYEGSPIKVTLATLKMVQPTVS  
LGGFEITPPVVLRLKCGSGPVHISGQHLVAEEDAEESEDEDEEDVLLGMSGKRSAPGGGNKVPQKKVKLDDEDDEDDDEDDEDD  
DDDFDEEEETEEKVPVKKSVRDTPAKNAQKSQNQNGKDLKPSTPRSKKGQESFKKQEKTPKTPKGSSVEDIKAKMQASIEKGGSPLKVEAK  
FINYVKNCFRMTDQEAIQDLWQWRKSL.

### ***In situ* Hi-C library preparation and initial data processing**

*In situ* Hi-C was performed as previously described<sup>35,79</sup> using ~2 million cells as starting material. After Hi-C library quality was assessed, each biological replicate ( $n = 2$ ) was sequenced on NextSeq500 (Illumina) sequencers (paired-end, 75 bp read length). In total, we obtained ~200 million read-pairs in total per condition. Hi-C data were processed using an in-house pipeline based on TADbit<sup>80</sup> as previously described.<sup>35,79</sup> In brief, after trimming and removing poor quality reads, contact pairs were mapped using a fragment-based strategy as implemented in TADbit. Mapped reads were filtered to remove non-informative contacts (e.g., self-circle, dangling-end, PCR duplicates). Contact matrices obtained were normalized for sequencing depth and genomic biases using OneD.<sup>81</sup>

### **Identification of subnuclear compartments**

To segment the genome into A/B compartments, normalized Hi-C matrices at 100kb resolution were corrected for decay as previously published, grouping diagonals when signal-to-noise was below 0.05.<sup>82</sup> Corrected matrices were then split into chromosomal matrices and transformed into correlation matrices using the Pearson product-moment correlation. The first component of a PCA (PC1) on each of these matrices was used as a quantitative measure of compartmentalization and H3K4Me2 ChIP-seq data was used to assign negative and positive PC1 categories to the correct compartments. If necessary, the sign of the PC1 (which is randomly assigned) was inverted so that positive PC1 values corresponded to A compartment regions and vice versa for the B compartment. To segment the genome into high resolution A/B compartments, we used CscoTool<sup>83</sup> to allow for rapid compartment analysis at 10 kb resolution, with computed C scores reflecting quantitative association with A (0–1) or B (–1 to 0) compartments for each bin. For differential CscoTool analysis, the average scores of the 2 replicates were calculated for each condition and directly subtracted.

### **Long-range interactions between CEBPA binding regions**

Hi-C matrices were generated at 10-kb resolution using HiCExplorer<sup>84</sup> and long-range interactions (2–10 Mb) between CEBPA binding regions were computed using the HiCExplorer tool *hicAggregateContacts*.

### **Identification of differential interactions between non-induced and 24h CEBPA induced B cells**

Hi-C matrices at 10 kb resolution were analyzed with Homer software<sup>85</sup> and the **analyzeHiC** tools using the following parameters (*-pvalue* 0.0001 and *-MaxDist* 10000000). The *Circos* option was used to visualize interactions specifically gained after 24h of CEBPA induction.

### **CEBPA interaction at the JUN locus**

Observed versus expected HiC matrices at 10 kb resolution were generated using HiC explorer after merging the 2 replicates for each condition.<sup>84</sup> Significant intrachromosomal interaction between the 10 kb bin harboring the CEBPA KO sites and all other bins harboring CEBPA binding sites were obtained using BEDTools.<sup>86</sup> For differential interaction analysis, the log2 fold changes between non-induced and CEBPA-induced cells were directly calculated by subtraction.

### **Gene expression analysis using RNA-seq data**

Reads were mapped using STAR<sup>87</sup> (standard options) and the Ensembl human genome annotation (GRCh38v27). Gene expression was quantified using STAR (–quantMode GeneCounts). Sample scaling and statistical analysis were performed using the R package DESeq2<sup>88</sup> (R 3.3.2 and Bioconductor 3.0). Log2-vsD (variance stabilized DESeq2) counts were used for further analysis unless stated otherwise.

### **ChIP-seq data analysis**

Reads were mapped to the reference genome build (human hg38, mouse mm10) using Bowtie2<sup>89</sup> with standard settings. Reads mapping to multiple locations in the genome were removed using SAMtools<sup>90</sup>; PCR duplicates were filtered using Picard (<http://broadinstitute.github.io/picard>). Bam files were parsed to deepTools<sup>91</sup> for downstream analyses and browser visualization. CEBPA and BRD4 peaks were identified using MACS2<sup>92</sup> with the *narrowpeaks* option. Peaks not called in both independent biological replicates were excluded in all subsequent analyses. Coverage of CEBPA peaks per TAD border was computed using BEDTools.<sup>86</sup> Coverage and binding heatmaps were performed using deepTools.<sup>91</sup> Analysis and gene association of the CEBPA peaks list were performed using GREAT.<sup>93</sup>

## **QUANTIFICATION AND STATISTICAL ANALYSIS**

Insight3 Software used for STORM image processing has been generated<sup>94</sup> and kindly provided by Dr Bo Huang (UCSF).

ImageJ 2.0.0 software used for microscopy imaging analysis can be found at: <https://imagej.nih.gov/ij/download.html>. MATLAB (MathWorks) software was used for STORM cluster analysis can be found at: <https://www.mathworks.com/products/matlab.html>.

All the statistical details of experiments can be found in the figure legends, including the statistical tests used, exact value of  $n$ , what  $n$  represents. All boxplots depict the first and third quartiles as the lower and upper bounds of the box, with a thicker band inside the box showing the median value and whiskers representing  $1.5 \times$  the interquartile range.

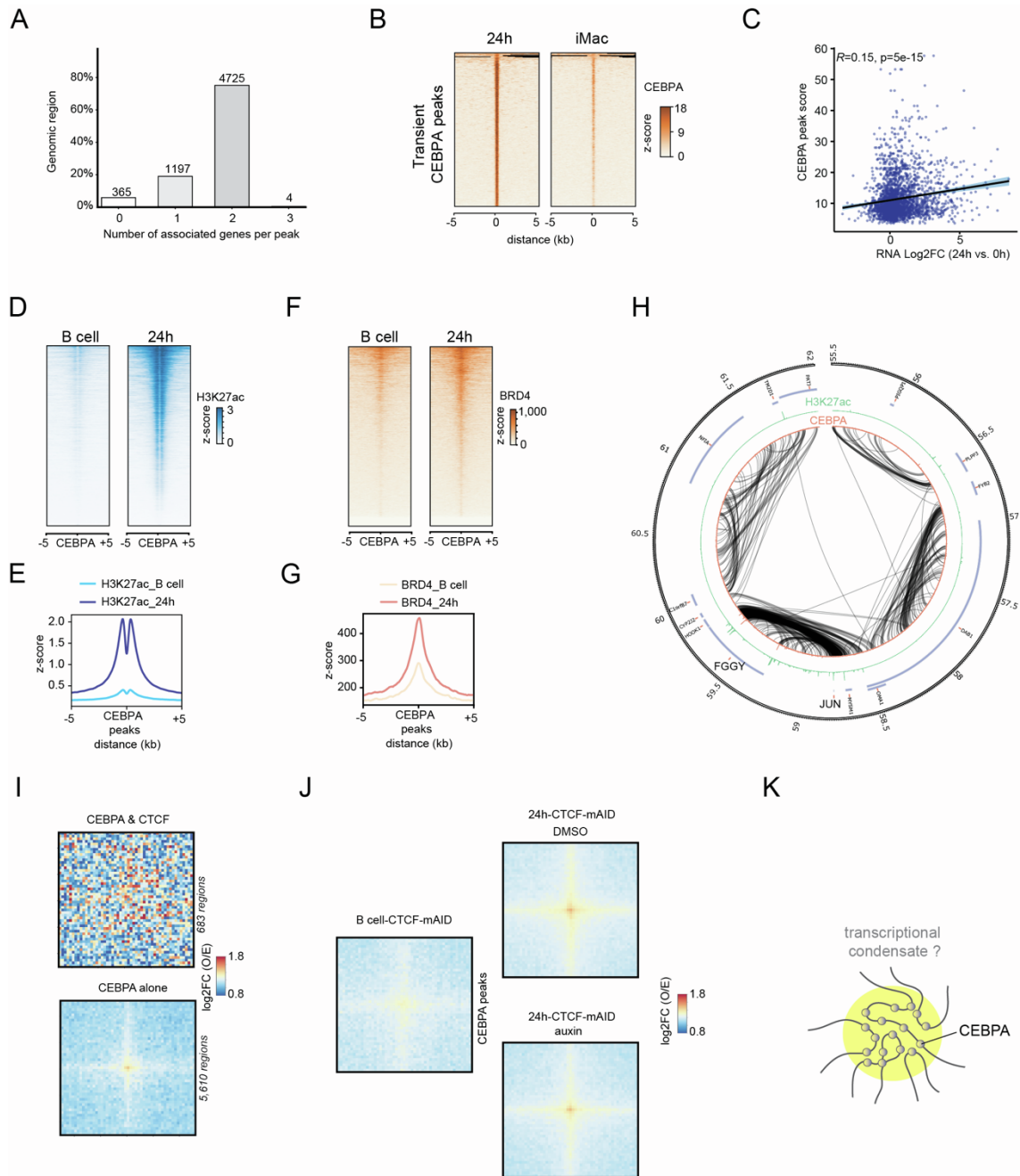
## Supplemental information

### **CEBPA phase separation links transcriptional activity and 3D chromatin hubs**

Marie Christou-Kent, Sergi Cuartero, Carla Garcia-Cabau, Julia Ruehle, Julian Naderi, Julia Erber, Maria Victoria Neguembor, Marcos Plana-Carmena, Marc Alcoverro-Bertran, Luisa De Andres-Aguayo, Antonios Klonizakis, Eric Julià-Vilella, Cian Lynch, Manuel Serrano, Denes Hnisz, Xavier Salvatella, Thomas Graf, and Grégoire Stik

## SUPPLEMENTAL INFORMATION

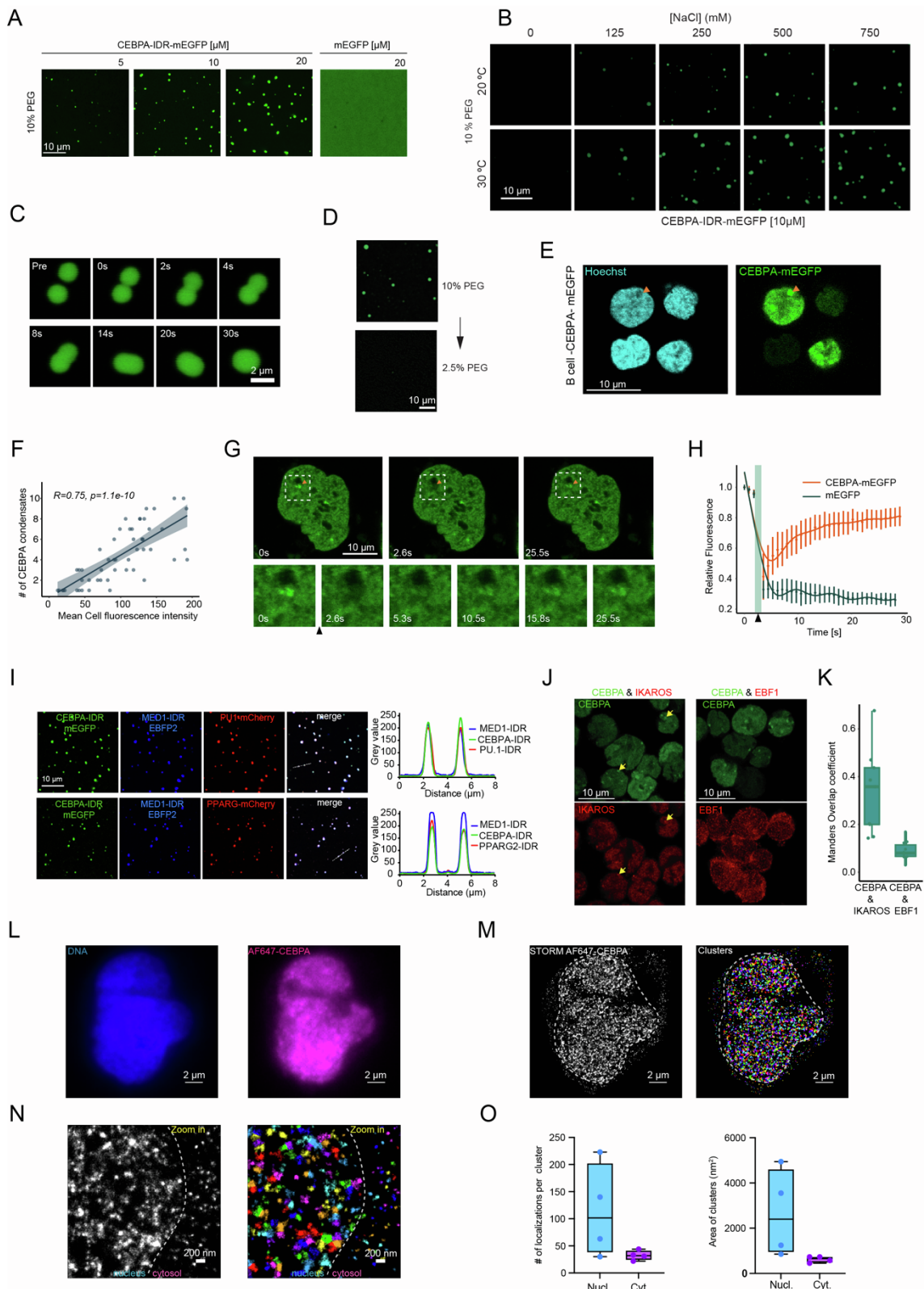
### SUPPLEMENTAL FIGURES



**Supplemental Figure 1. CEBPA-driven chromatin hubs in transdifferentiating B cells are transient, transcriptionally active and regulate multiple genes. Related to Figure 1.**

(A) CEBPA ChIP-seq peak annotation showing the number of genes associated with each CEBPA-bound region (raw numbers indicated above bars). (B) Heatmap of CEBPA binding centered on CEBPA transient peaks during iMac transdifferentiation. Black lines

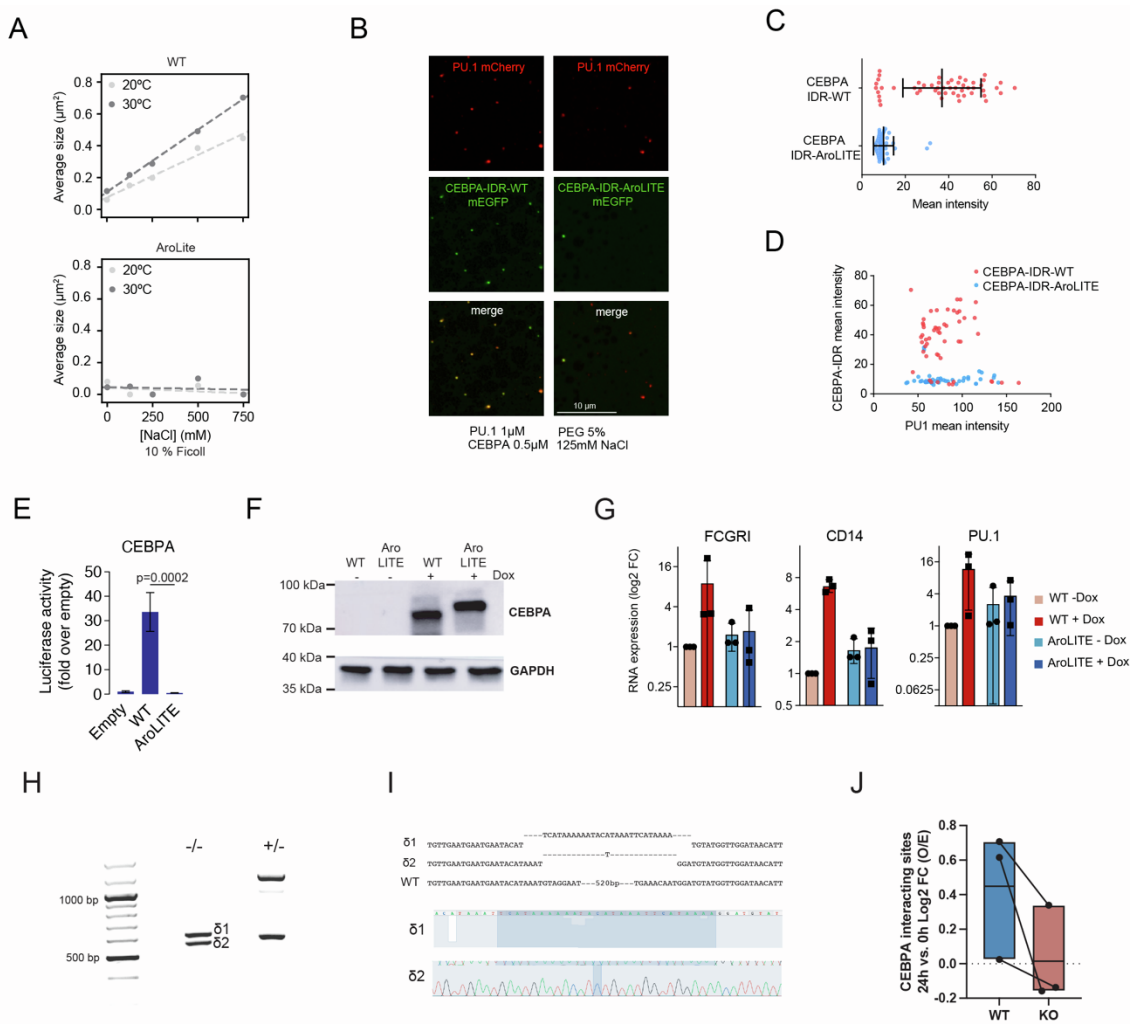
represent segments of the genome with no read coverage. (C) Scatter plot showing the correlation between changes in RNA levels before and 24h after CEBPA induction of genes in proximity (< 50kb) to CEBPA peaks (relative to Figure 1D) and the enrichment score of the CEBPA peaks detected at 24h. (D) H3K27ac and BRD4 (F) occupancy at CEBPA peaks (defined at 24h CEBPA expression) at 24h. (E) Quantification of H3K27ac and BRD4 (G) occupancy at CEBPA sites shown in Figure S1D and F. (H) Circular interaction map of region shown in Figure 1F displaying differential interactions gained in B cells after 24h CEBPA induction (defined using Homer software) and CEBPA and H3K27a ChIP-seq tracks. (I) Aggregate heatmaps of normalized genome-wide Hi-C signals at 24h of CEBPA induction centered on CEBPA peaks overlapping (above) or not overlapping CTCF peaks (below). (J) Aggregate heatmaps of normalized genome-wide Hi-C signals at 0h and 24h of CEBPA induction centered on CEBPA peaks in the context of acute CTCF depletion (CTCF-mAID-auxin) or in control conditions (CTCF-mAID-DMSO). Thresholds were set to display interactions between sites at genomic distances of 2-10 Mbp (data at 10 kb resolution, heatmaps plot 250 kb upstream and downstream of the bound regions; O/E=Observed over Expected). (K) Proposed mechanism of CEBPA forming chromatin hubs through a phase separation process.



**Supplemental Figure 2. Further characterization of CEBPA PS. Related to Figure 2.**

(A) Phase separation of recombinant CEBPA-IDR-mEGFP with increasing protein concentration in the presence of PEG 4000 (10%) as a crowding agent, 125 mM NaCl

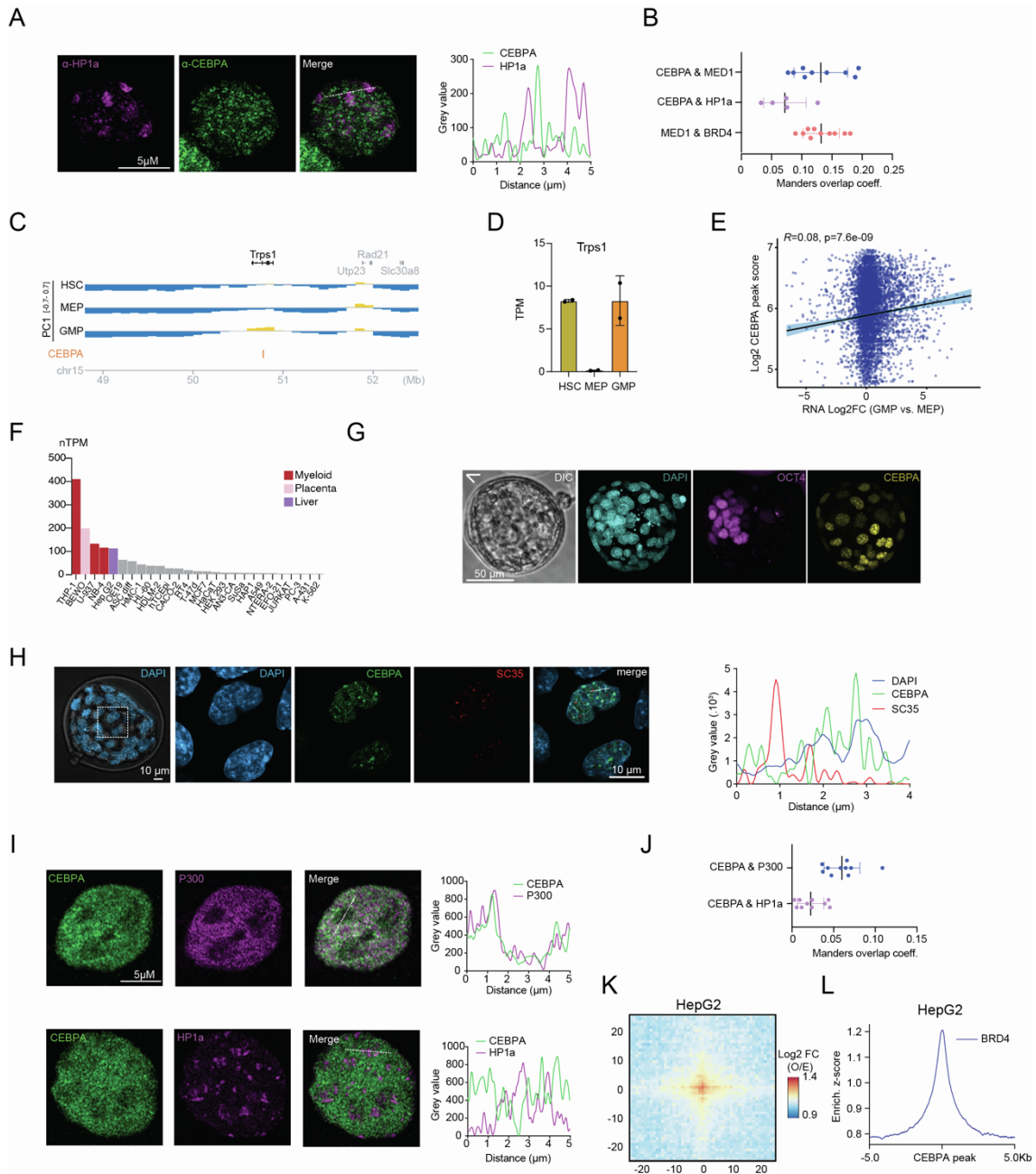
and 10% glycerol. (B) Salt dependence of CEBPA-IDR-mEGFP phase separation at 10 $\mu$ M protein concentration in the presence of PEG 4000 (10%) at 20°C and 30°C. Representative images showing: (C) a fusion event of CEBPA-IDR-mEGFP droplets over time (s, second), (D) the reversibility of CEBPA-IDR droplet formation after PEG dilution. (E) Images showing CEBPA condensates at 24 hrs post doxycycline in live cells under confocal microscopy (scale bar = 10  $\mu$ m). Orange arrowhead highlights a CEBPA-mEGFP punctum occupying non-dense chromatin. (F) Correlation between the number of CEBPA-mEGFP large puncta and the mean mEGFP fluorescence intensity per cell in cells infected with CEBPA-mEGFP. (G) FRAP of CEBPA-mEGFP large puncta formed in live HepG2 cells 24h after transfection with CEBPA-mEGFP. The photobleached droplet is highlighted in a yellow box. Images show signal recovery over time after photobleaching (indicated by a black arrow). (H) Relative fluorescence recovery after photobleaching for CEBPA-IDR-mEGFP puncta (n=10) and control mEGFP (n=4) in transfected HepG2 cells. (I) *In vitro* co-phase separation of CEBPA-IDR-mEGFP with MED1-IDR-EBFP2 and PPARG-mCherry or PU1-mCherry, all at 3  $\mu$ M with 10% PEG 400, 125 mM NaCl and 10% glycerol. (J) CEBPA-mEGFP- transduced RCH cells, immunostained for IKAROS or EBF1. Yellow arrows indicate co-localised CEBPA and IKAROS puncta. (K) Quantification showing the overlap of CEBPA-mEGFP puncta with IKAROS and EBF1 puncta in CEBPA-mEGFP RCH cells (as in Figure S2J). (L) 24h-CEBPA induced BLaER cell immune-stained for DNA (in blue) and CEBPA (magenta) visualized in conventional microscopy mode before Stochastic Optical Reconstruction Microscopy (M) Same cell as in panel M visualized by Stochastic Optical Reconstruction Microscopy for CEBPA signal shown in white (left) and CEBPA clusters identified by cluster analysis are pseudo colored (right). (N) Zoom in of image shown in panel M. (O) Quantification of the number of localizations per cluster (left) and the area (right) of the CEBPA clusters in the nucleus (Nucl.) and the cytosol (Cyt.).



**Supplemental Figure 3. Trans- and Cis- mutation of CEBPA alter its ability to form shared condensates with PU1, its transcriptional activity and its ability to rearrange chromatin. Related to Figure 3.**

(A) Quantification of the average CEBPA-IDR-WT and -AroLITE droplet size as a function of salt concentration at 20 and 30°C with Ficoll used as crowding agent. (B) Representative images from droplet assays to compare the co-phase separation of CEBPA WT or AroLITE IDR-mEGFP fusion proteins (at 0.5  $\mu\text{M}$ ) and PU.1-mCherry (at 1  $\mu\text{M}$ ). (C) Quantification of the mean mEGFP fluorescence intensity within PU.1-mCherry droplets for CEBPA-IDR WT and AroLITE. ( $n= 52/51$  droplets WT/AroLITE, respectively). (D) Scatter plot of PU.1-mCherry mean intensity against CEBPA-IDR-mEGFP mean intensity for WT and AroLITE per droplet. (E) Results of luciferase reporter assays in HEK293T cells. Luciferase values were normalized against an internal Renilla control, and the values are displayed as fold change over the activity measured using an empty vector. Data are displayed as mean  $\pm$  SD. Data are from four biological replicates with three technical replicates each. P-values are from Student's t-tests. (F) Western blot

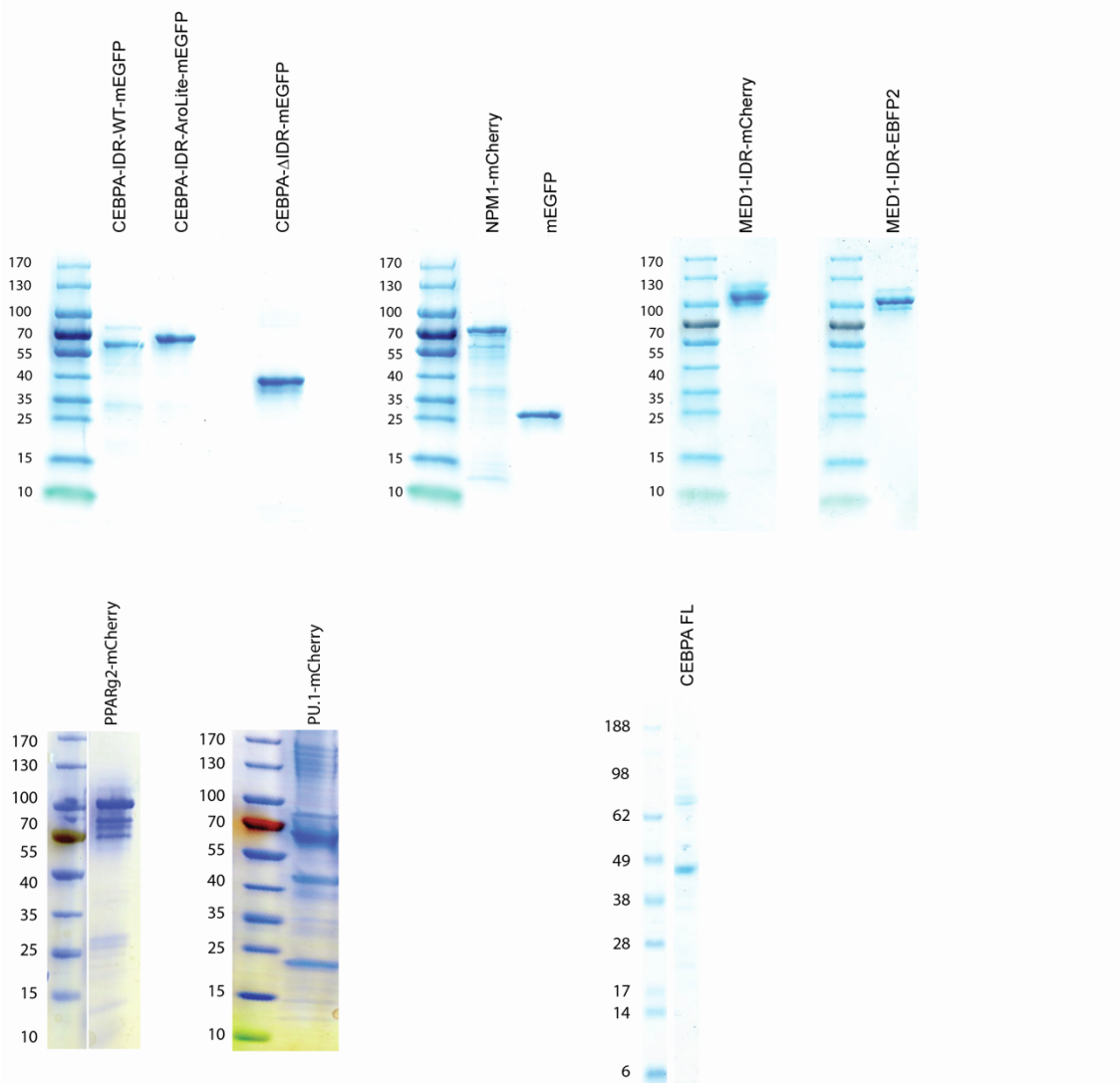
analysis of FL CEBPA in RCH-ACV-rtTA cells transduced with CEBPA-WT-mEGFP and CEBPA-AroLITE-mEGFP before or after 24h doxycycline (Dox) treatment. GAPDH was used as a loading control. (G) Expression levels measured by qRT-PCR of macrophage markers FCGRI, CD14 and PU1 normalized to GUSB in doxycycline-inducible CEBPA-WT or CEBPA-AroLITE RCH-rtTA cells, with and without doxycycline treatment. (H) Electrophoresis on a 1% agarose gel showing the PCR amplification at the JUN/FGGY locus of the homozygous KO clone and an example of a heterozygous clone. (I) Sequencing of PCR amplicons of the KO<sup>-/-</sup> clone showing the ~520 bp deletions in the targeted region. (J) Log2 fold change (FC) in interactions of CEBPA-containing bins at the JUN/FGGY locus (depicted as red lines in Figure 3H) comparing 24h CEBPA-induced and non-induced (0h) WT or KO B cells (O/E=Observed over expected).



**Supplemental Figure 4. CEBPA forms foci in mouse embryos and liver cells and is associated with active chromatin regions. Related to Figure 4.**

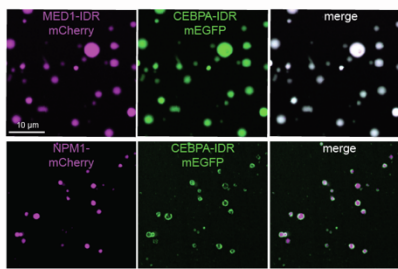
(A) Representative image of primary granulocyte/monocyte precursors (GMPs) sorted from MED1-GFP mouse bone marrow, immunostained for CEBPA and HP1a and imaged at super resolution. A line scan analysis of the merged image is depicted on the right. (B) Quantification showing the overlap of CEBPA with MED1 (GFP) or HP1a and MED1 (GFP) with BRD4 in GMPs isolated from MED1-GFP mice (related to Figure 4C and S4A). (C) Compartmentalization in an example region containing the gene *Trps1* (Transcriptional repressor GATA binding) on chromosome 15 across HSCs, MEPs and GMPs. GMP CEBPA sites are shown underneath in orange. (D) RNA expression data

for *Trps1* across the 3 hematopoietic cell types. (E) Scatter plot showing the correlation between changes in RNA levels of genes in proximity (< 50kb) to CEBPA peaks in MEPs and GMPs and the enrichment score of the CEBPA peaks detected in GMPs (related to Figure 4I). (F) CEBPA expression data across human cell lines (nTPM: number of transcripts per million, source: proteinatlas.org). (G) Mouse blastocysts immunostained for CEBPA (trophectoderm) and OCT4 (inner cell mass). (H) Enlargement of mouse trophectoderm at super resolution showing CEPBA and splicing factor sc35 puncta (from the region indicated by a dashed box in the left image). Line scan analysis of the merged image is depicted on the right. (I) Representative image of HepG2 cells immunostained for CEBPA and P300 or HP1a and imaged at super resolution. A line scan analysis of the merged image is depicted on the right. (J) Quantification showing the overlap of CEBPA with P300 or HP1a in HepG2 cells (related to Figure S4I). CEBPA-immunostaining in liver cell line HepG2 visualized by super resolution microscopy. (K) Aggregate heatmaps of normalized genome-wide Hi-C signals in HepG2 cells centered on HepG2 CEBPA peaks. Thresholds were set to display interactions between sites at genomic distances of 2-10 Mbp (data at 10 kb resolution, heatmaps plot 250 kb upstream and downstream of the bound regions. (L) Quantification of BRD4 occupancy at CEBPA sites in HepG2.

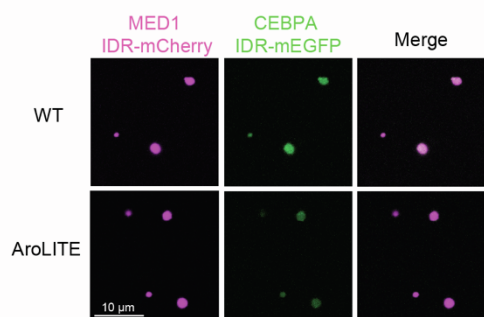


**Supplemental Figure 5. Controls images of the Coomassie-stained gels obtain for each protein purification, Related to STAR Methods.**

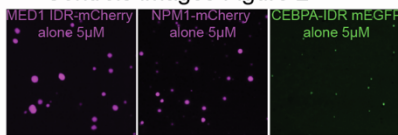
Images Figure 2



Images Figure 3



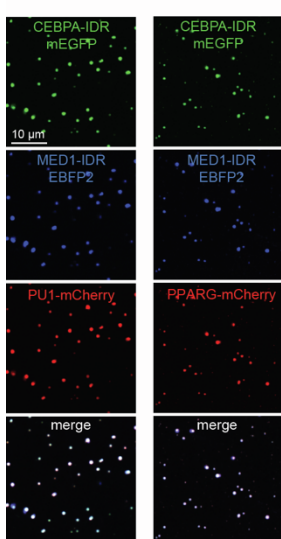
Controls images Figure 2



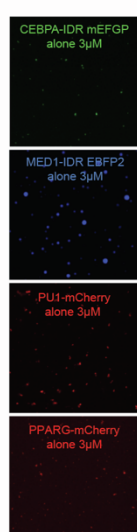
Controls images Figure 3



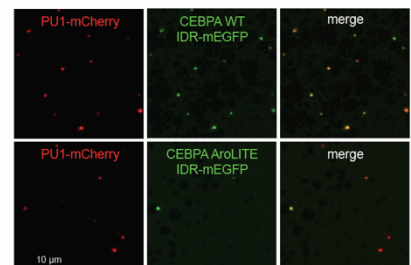
Images Supp. Figure 2



Controls images Supp. Figure 2



Images Supp. Figure 3



Controls images Supp. Figure 3



**Supplemental Figure 6. Controls images of the co-phase separation assays showing each protein at the same conditions, Related to STAR Methods.**

Name	Sequence (5'-3')
GUSB fw	CACCAAGGATCCACCTCTGAT
GUSB rev	TCCAAATGAGCTCTCCAACC
CD14 fw	GATTACATAAACTGTCAGAGGC
CD14 rev	TCCATGGTCGATAAGTCTTC
ITGAM fw	GGGGTCTCCACTAAATATCTC
ITGAM rev	CTGACCTGATATTGATGCTG
CSFR1 for	TCCAAAACACGGGGACCTATC
CSFR1 rev	CGGGCAGGGTCTTGACATA
FCGRI fw	CCTTGAGGTGTCATGCGTG
FCGRI rev	AAGGCTTGCCATTTCGATAGT
VPREB3 fw	GGGGACCTTCCTGTCAGTTT
VPREB3 rev	GGGGACCTTCCTGTCAGTTT
PU.1 fw	GGAGAGCCATAGCGACCATT
PU.1 rev	CTGGAGCTCCGTGAAGTTGT
EBF1 fw	TGCTACTCCCTGTATGAAAG
EBF1 rev	ATGGTACCGAATATGACCTG

**Supplemental Table 1. Oligonucleotides used for qRT-PCR experiments, Related to STAR Methods.**